Chemical Sensing in Spatial/Temporal Domains

Takamichi Nakamoto, and Hiroshi Ishida

Chem. Rev., **2008**, 108 (2), 680-704 • DOI: 10.1021/cr068117e

Chemical Sensing in Spatial/Temporal Domains

Takamichi Nakamoto*,† and Hiroshi Ishida‡

Graduate School of Science and Engineering, Tokyo Institute of Technology, 2-12-1 Ookayama, Meguro-ku, Tokyo 152-8552, Japan, and Department of Mechanical Systems Engineering, Tokyo University of Agriculture and Technology, 2-24-16 Nakacho, Kogahei, Tokyo 184-8588, Japan

Received May 14, 2007

Contents

1. Introduction

Sensors are devices to receive physical or chemical signals and to convert them into electrical signals. Physical signals are carried by waves such as electromagnetic, optical, and acoustic ones. Sensing technology for physical signals has been well-understood and has already been established. On the other hand, sensing technology for chemical signals, which are carried by chemical substances, is not matured.

* Corresponding author. Tel.: +81-3-5734-2579. Fax: +81-3-5734-2828. E-mail: nakamoto@mn.ee.titech.ac.jp.
† Tokyo Institute of Technology.
‡ Tokyo University of Agriculture and Technology.

It is thought that chemical substances are moved by molecular diffusion. However, diffusion velocities of gas molecules are too slow to transport chemical signals under many conditions. The transport of chemical substances onto chemical sensors is actually governed by fluid dynamics. Fluid dynamics offers two aspects such as a signal in spatial domain and one in time domain. A signal in spatial domain is tightly coupled with a plume, a flowing trail of a chemical substance.

Although the electromagnetic and acoustic waves mainly propagate straight and their behaviors are easily predicted, it is difficult to predict the behavior of the plume. Thus, it is helpful to see the plume dynamics so that people can understand the plume behavior in spatial domain. Then, the gas distribution can be measured using a homogeneous sensor array. The two types of sensor arrays such as sparse and packed sensor arrays are available. The sparse sensor array can show the global behavior of the plume, whereas the packed one reveals the local detailed behavior of the plume.

Although the measurement of gas distribution is the typical method to reveal the chemical-signal behavior in spatial domain, one of the recent topics is the plume generated in a virtual environment, where people perceive sensory stimuli even if they do not stay in the actual environment. In virtual reality, people can perceive an object with smell. The direction to an odor source, the feeling of approaching or going away from it, might be realized even if the actual smell source is not in front of people; it is difficult for a chemical sensor to follow the true dynamic concentration change of the chemical substance.

Generally, temporal behavior of a chemical sensor has not been well-studied in comparison with steady-state response. However, the temporal signal sometimes has information of chemical substance. Thus, the technique to know the sensor dynamics such as time constant is required. In some cases, time constant must be obtained even if the concentration profile is irregular and is not known. In some cases, the peaks of the chemical signal over time provide information of chemical substance.

The temporal data from preconcentrator is also useful to obtain information on the chemical substance. In addition to raising the sensitivity, the preconcentrator with variable temperature can be used to enhance the pattern separation among odor samples.

The sensing in both spatial and time domains is complicated. Although there have been many works in a single domain, a limited number of works have been addressed to combining both domains. The straightforward method to understand the combination of both domains is to observe change in spatial distribution with time. Another approach

10.1021/cr068117e CCC: $71.00
Published on Web 01/26/2008

Takamichi Nakamoto received his B.E. and M.E. degrees from the Tokyo Institute of Technology in 1982 and 1984, respectively. In 1991, he earned his Ph.D. degree in Electrical and Electronic Engineering from the same institution. He worked for Hitachi in the area of VLSI design automation from 1984 to 1987. In 1987, he joined the Tokyo Institute of Technology as a research associate. He has been an Associate Professor at the Department of Electrical and Electronics Engineering, Tokyo Institute of Technology, since 1993. From 1996 to 1997, he was a visiting scientist at the Pacific Northwest Laboratories, Richland, WA. His research interests cover chemical sensing systems, acoustic wave sensors, olfaction in virtual reality, and LSI design.

Hiroshi Ishida was born in Morgantown, WV, in 1970. He received M.E. and Ph.D. degrees in electrical and electronic engineering from the Tokyo Institute of Technology, Tokyo, Japan, in 1994 and 1997, respectively. From 1997 to 2004, he was a research associate of the Tokyo Institute of Technology. From 1998 to 2000, he visited the School of Chemistry and Biochemistry, Georgia Institute of Technology, Atlanta, GA, as a Postdoctoral Fellow. In 2004, he joined the Department of Mechanical Systems Engineering at the Tokyo University of Agriculture and Technology, Tokyo, Japan, where he is currently an associate professor. In 2007, he was a visiting researcher in the AASS Research Centre, Örebro University, Sweden. His research interests are in biomimetic electronics with emphasis on chemical sensors and their applications in robotics.

is to see the correlation of signal features in time domain with several locations. The frequency analysis of the signals also provides us with useful information about an odor-source location.

This paper covers dynamic behavior of a chemical sensor both in spatial and temporal domains. First, the spatial domains such as plume behavior and method of gas-distribution measurement are described. Moreover, presentation of an odor source in a virtual environment is explained.

Another part is temporal-response behavior of a gas sensor. The sensor dynamics model and the analysis method are described. Then, the analysis in the frequency domain and temporal data from a preconcentrator with variable temperature are explained. The final part is the sensing in both spatial and time domains. Observation and analysis techniques for dynamic behavior in the liquid phase are described.

2. Spatial Domain

We focused on the chemical sensor signals in spatial domain. First, the plume behavior and its observation method using an optical tracer are described. Then, the methods of the gas-distribution measurements using the packed sensor array for obtaining the direction to the gas source, the sparse sensor array for obtaining the global information, and the optical method for obtaining the information remotely are explained. Moreover, the virtual environment where people can perceive spatial information of odor is introduced in this section.

2.1. Plume Behavior and Analysis Method

Gas molecules are carried by air flow and distributed by turbulence. The transport of chemical substances can be visualized by a tracer such as smoke. Smoke from a chimney moves in a downwind direction, and the smoke density is dispersed and made thin by turbulence. The chemical substances emanating from the chimney are moving in the same manner as the smoke because the molecular diffusion velocities are smaller than the wind velocity.

In environmental chemistry, air or water is analyzed at sites and in a laboratory. The pollutant is carried by a plume in air or water flow, and its concentration fluctuates because of the turbulence. The typical shape of the plume is illustrated in Figure 1. The plume spreads gradually from an odor source along the downwind direction. Thus, the concentration gradually decreases according to the distance from the odor source along the wind direction. However, the concentration gradient is steep across the wind direction. It is difficult to determine the direction to the odor source using only the concentration gradient because the concentration gradient along the wind direction is small and often within the noise level.[1] Note that the plume shape in Figure 1 is the averaged one over time. Since its actual shape is highly fluctuated due to the turbulence, the noise level is high when we measure the concentration gradient along the wind direction.

The plume behavior is governed by the fluid dynamics, which is solved using the Navier−Stokes equation. Although the numerical approach is often used to obtain the gas-concentration distribution, it consumes a long time and plenty of computational resources. Thus, a number of models for plume were proposed. The simple mathematical model of the time-averaged plume shape is available and can be expressed as the solution of the Fickian turbulent diffusion equation when the time-averaged wind speed is constant and the wind turbulence is isotropic and homogeneous.[2] The instantaneous plume is very thin. The time-averaged plume shape is wider because the fluctuated plume is integrated over time, as is shown in Figure 2. Semiempirical Gaussian plume models assume a Gaussian distribution of mean concentration in the plane perpendicular to the plume center line.[3] The growth of the plume width and the height are determined by the parameters called dispersion coefficients. The values of those constants for large-scale outdoor plumes under various atmospheric stability conditions were obtained from a number of experiments.[4] Although the Gaussian plume models are widely used for assessing the distribution

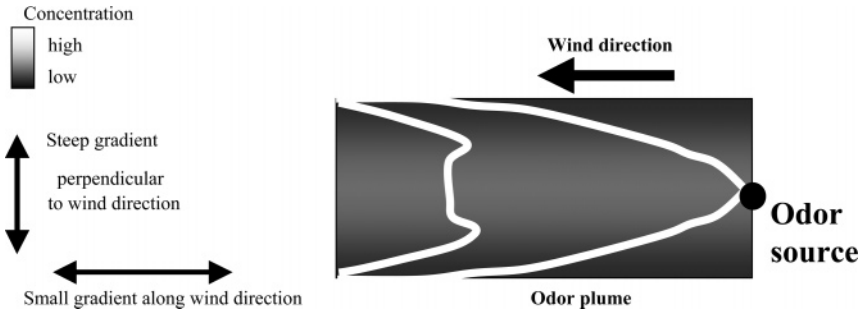

Figure 1. Typical plume shape.

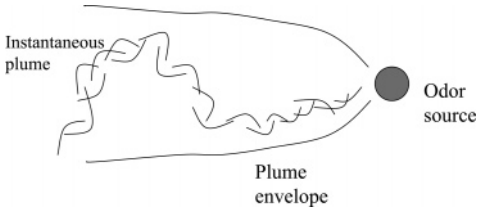

Figure 2. Plume fluctuation.

of gaseous pollutants, they lack an important feature of real plumes, i.e., meanderings. Puff models assume that a plume is composed of a series of puffs released from the source over time. A Gaussian concentration distribution is generally assumed in each puff, but now the position of each puff is free to move according to the local wind direction. A variety of plume models are also proposed and used to describe other features of real plumes, e.g., rise of a buoyant plume and chemical reaction in plumes,[5] but providing a detailed description of each model is beyond the scope of this review.

2.2. Plume Observation Method

Study of the dynamic behavior of gas flow is laborious work because air turbulence is complicated even if the fluid-dynamics analysis is performed on a supercomputer. Visualization of dynamic gas distribution using a tracer is a more realistic way to understand the dynamic behavior of the plume. A variety of simulations for localizing an odor source can be performed if the real-time image of the gas flow is obtained through visualization.

An optical tracer can be used to visualize the plume. The tracer is a visible light particle that behaves in the same manner as that of the fluid. When the tracer is emitted from the source together with the odor, we can know the odor distribution when we visually observe the tracer distribution.

In the gas phase, titanium tetrachloride and dry ice are used. However, they are toxic or dangerous when sufficient smoke required for the charge-coupled device (CCD) camera is used. Another candidate is oil mist, often generated by a smoke machine. It is typically used for entertainment in TV show, theater, concert, etc. Since plenty of smoke is required to obtain the clear image using a video camera, the smoke machine is appropriate from that point of view. However, the oil is deposited over the place close to the smoke machine after the experiment.

The white smoke of joss sticks can be used as a tracer.[6] Smoke particles from burning joss sticks are so small that the fall velocity is much smaller than typical wind velocity. The diameter of a joss stick particle is $\sim$1 μm, and it is easy to track the behavior of the gas molecule under the environment of typical wind velocity. It does not track the gas molecule under the environment without wind.

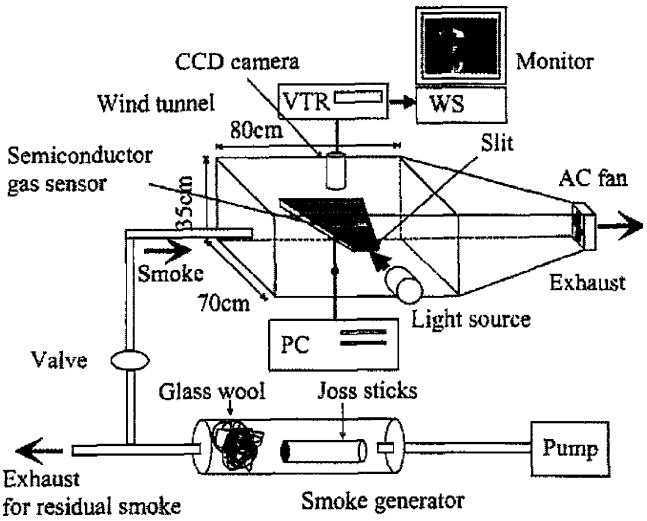

Figure 3. Plume observation method. Reprinted with permission from ref 6. Copyright 1998 Elsevier Science.

The advantage of joss stick (incense) is that it works as both tracer and gas molecule. When we observe the plume behavior together with gas sensor response, only the single source is required. Although joss stick is good for visualizing plume, hollow microfiber polymer particles are sometimes used.[7] Since the polymer particle does not produce the signal by itself, a gas sensor does not respond to it. Thus, it can be mixed with any vapor.

Next, the visualization system is described. The image of the 2D optical tracer distribution corresponding to the 2D gas distribution at the light sheet is captured by a video camera. Since it is difficult to obtain a real-time 3D image, the light sheet is illuminated to obtain the two-dimensional image, as is illustrated in Figure 3. Smoke is spouted from the nozzle in a wind tunnel, and the height of the light sheet is adjusted so that most of the smoke can be visualized. The image of the light scattered by smoke particles is captured by the video camera. That image is recorded by a VCR (video cassette recorder) and is transferred to a computer. Although there are many products of video cameras, the video camera without AGC (auto gain control) was selected because the light intensity was proportional to the gas concentration when AGC was off. We can currently obtain the real-time image in a digital format using a DVC (digital video camera), although the system in Figure 3 is a little old.

The light sheet was generated by the strong illumination through the slit (60 mm in width, 2 mm in height). Although the xenon lamp (500 W) was previously used as the light source, most of light energy was discarded. A combination of a semiconductor laser with cylindrical lens or high-power

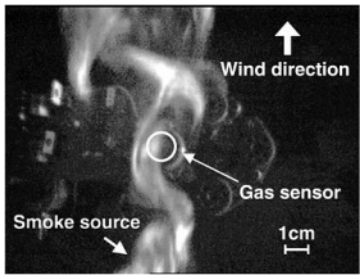

Figure 4. Instantaneous smoke image visualizing gas concentration. Reprinted with permission from ref 1. Copyright 1999 American Chemical Society.

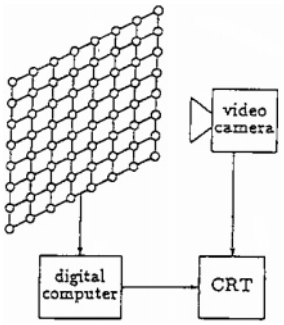

Figure 5. Large sensor array and visualization system. Reprinted with permission from ref 9. Copyright 1992 Elsevier Science.

light-emitting diode (LED) array is a good candidate to realize bright light sheet.

An example of instantaneous smoke image visualizing gas concentration is shown in Figure 4. This is the image just above the semiconductor gas sensor in a wind tunnel. The smoke of joss stick emitted into the wind tunnel was carried by the wind toward the exhaust, and the aerial smoke trail was formed in the downwind direction. Since the shape of this trail was disordered because of the wind turbulence, the instantaneous gas concentration at the sensor place changed rapidly. The temporal behavior of the sensor will be discussed in section 3.1.

2.3. Gas-Distribution Measurement

Gas distribution can be measured using many sensors. There are two types of gas-distribution measurement systems. One is a sensor array packed into a small region, and the other is an array of sensor nodes located away from each other. We discuss both types of sensor arrays for gas-distribution measurements.

2.3.1. Measurement of Spatial Gas-Distribution Change by a Large Sensor Array

The initial approach to measure the spatial gas distribution was performed by Yamasaki and Hiranaka.[8,9] They made the sensor array composed of the same tin oxide gas sensors as is illustrated in Figure 5. 8 × 8 sensors were spatially placed, and the distance between the two was 20 cm. The outputs of the sensors were digitally processed to form images of the spatial gas distribution on a computer screen. The image of the scene was taken by a video camera, and these two images were overlaid and displayed on a screen for easily understanding the gas field. The gas-distribution image was formed by linear or bilinear interpolation.

The vapor from the liquid source placed at the center of the sensor array is visualized as is shown in parts a−c of Figure 6. Figure 6a shows the overlaid image of ethanol vapor. The gas distribution is expressed using grayscale, and the white cloud indicates the position of the vapor source. Figure 6b shows the ethyl ether diffusing in the vertical direction. Figure 6c shows the distribution of odor from a human body. The odor seemed to come from his socks. It was found that the spatial gas distribution could be easily grasped because of the overlaid image from the video camera.

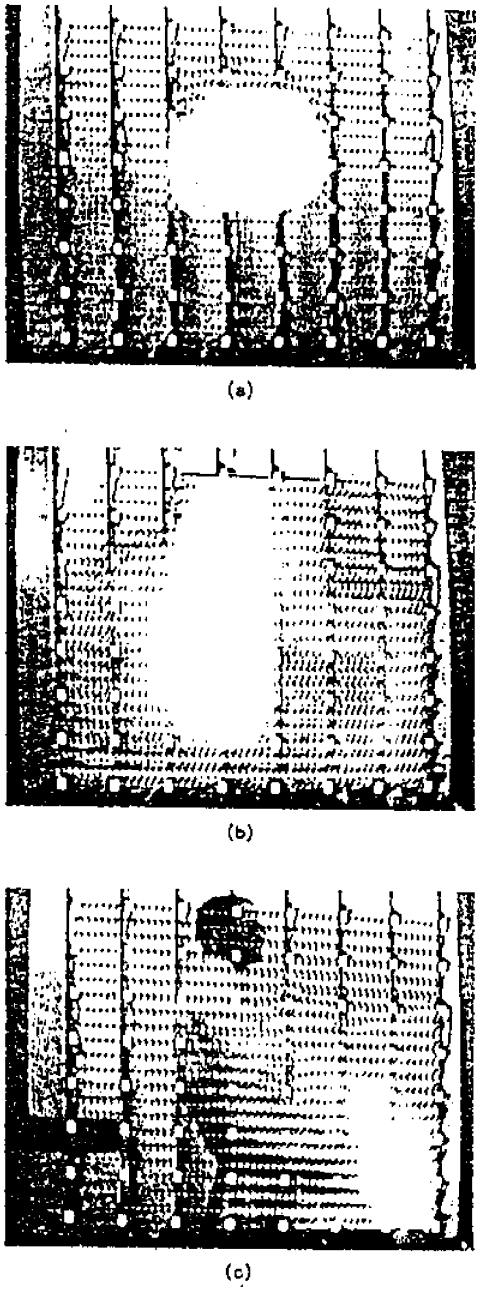

Figure 6. Visualization result using a large sensor array: (a) overlaid image of ethanol vapor, (b) overlaid image of ethyl ether vapor, and (c) odor from a human body. Reprinted with permission from ref 9. Copyright 1992 Elsevier Science.

2.3.2. Gas-Distribution Measurement by Packed Sensor Array

2.3.2.1. Strategy. The first type of gas sensor array is a two-dimensionally packed sensor array as is illustrated in Figure 7. This sensor array is used to measure local gas distribution. The temporal change of local gas distribution provides the information of the direction toward the gas source.

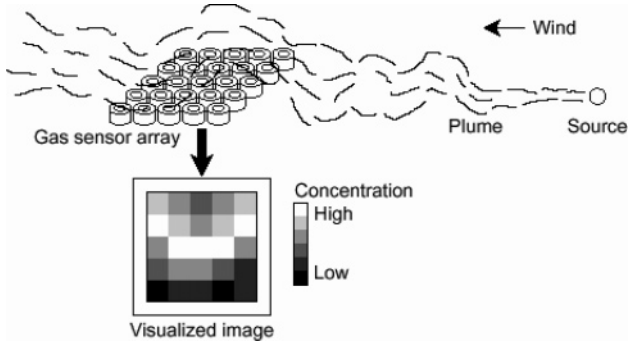

Figure 7. 2D packed sensor array.

The strategy to search for the odor source using a gas sensor together with wind direction sensor is often used.[10,11] Upon the basis of that strategy, a robotic system can trace the plume in the upwind direction. However, the capability of this system is limited by the low sensitivity of the anemometric sensors used for obtaining the wind direction. The typical wind velocity in an ordinary room, a few cm/s, is not detectable by the sensors on the system. The capability of searching for the gas/odor source can be improved if the direction toward the source is obtained not using the anemometric sensor.

One of the methods to obtain the direction toward the odor source is to use the image flow of the visualized gas cloud. When we use a two-dimensional homogeneous gas sensor array, the gas-concentration distribution over the sensor array is visualized as a grayscale image. The structure of the plume in a turbulent wind field looks like a gas cloud composed of many fragments, as is shown in Figure 7. Then, the gas flow direction is obtained from the movement of the visualized gas cloud. This method is effective under the environment of low wind speed. Moreover, redundant information from the sensor array may make the system more reliable under the environment with large fluctuation due to the air turbulence. Although the instantaneous and local gas flow is not always the same as the global one, the approach of the sensor array enhances the robustness of the flow direction estimation by obtaining the averaged direction from the redundant information.

2.3.2.2. Study of Response-Speed Influence by Simulation. The requirement for gas sensors to realize a gas flow imaging system is both sensitivity and response speed. The recovery speed from the response is also important. The first trial was to make the semiconductor gas sensor array.[12] 5 × 5 gas sensors were placed within the area (55 mm × 55 mm). However, the gas flow observed using the sensor array was not so clear, and the brightness of the whole image changed because of the slow recovery speed. The influence of the sensor speed can be understood when the simulation is performed. The gas concentration at each sensor location is obtained using the plume-observation technique in Figure 3.

Smoke of joss sticks was introduced into the wind tunnel as a tracer to simulate a gas field, and the video data captured by a CCD camera were transferred to the computer. Then, an array of virtual semiconductor gas sensors was then assumed to be placed on the visualized gas distribution in the wind tunnel. Then, the transfer function from gas concentration to a sensor response was applied at each point in the array. As a result, an image from a virtual gas sensor array was obtained.[13]

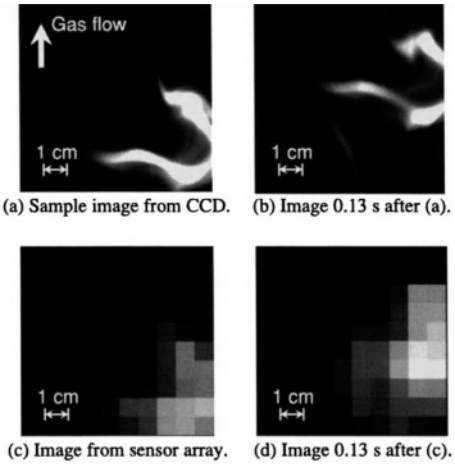

Figure 8. Example of gas flow images. Reprinted with permission from ref 13. Copyright 2000 Elsevier Science.

The transfer function consists of two terms with different time constants as described later in section 3.2. The two time constants change in response and recovery phases. The obtained time constants were 0.33 and 0.15 s in the response phase and 15.12 and 0.1 s in the recovery phase when the semiconductor gas sensor (TGS800, Figaro) was used.

Examples of images obtained from a 10 × 10 virtual sensor array are shown in Figure 8 parts c and d with the original smoke images captured by a CCD camera in Figure 8 parts a and b. The gas flow direction can be obtained by comparing the successive images. Although the convention effect might influence the plume, it was not clearly observed in these figures.

2.3.2.3. Method of Estimating Gas-Flow Direction. Here, the method of estimating the gas-flow direction using a 2D packed sensor array is described. The gas flow vector $\mathbf{v} = (v_x, v_y)^T$ is obtained by using the optical flow constraint equation expressed as

$$\frac{\partial c}{\partial x} v_x + \frac{\partial c}{\partial y} v_y + \frac{\partial c}{\partial t} = 0 \tag{1}$$

where c is gas concentration. The flow velocity is estimated by applying the least-squares method to the discrete form of eq 1.

When an array is composed of N sensors, the following equations are valid assuming that u and v are constant within the array.

$$\begin{aligned}
\left.\frac{\partial c}{\partial x}\right|_1 v_x + \left.\frac{\partial c}{\partial y}\right|_1 v_y &= -\left.\frac{\partial c}{\partial t}\right|_1 \\
\left.\frac{\partial c}{\partial x}\right|_2 v_x + \left.\frac{\partial c}{\partial y}\right|_2 v_y &= -\left.\frac{\partial c}{\partial t}\right|_2 \\
&\vdots \\
\left.\frac{\partial c}{\partial x}\right|_N v_x + \left.\frac{\partial c}{\partial y}\right|_N v_y &= -\left.\frac{\partial c}{\partial t}\right|_N
\end{aligned} \tag{2}$$

where $\partial c/\partial x|_i$ and $\partial c/\partial y|_i$ are the concentration gradients along x and y at sensor i.

When X and $\mathbf{y}$ are defined as

$$X = \begin{bmatrix} \left.\frac{\partial c}{\partial x}\right|_1 & \left.\frac{\partial c}{\partial y}\right|_1 \\ \left.\frac{\partial c}{\partial x}\right|_2 & \left.\frac{\partial c}{\partial y}\right|_2 \\ \vdots & \vdots \\ \left.\frac{\partial c}{\partial x}\right|_N & \left.\frac{\partial c}{\partial y}\right|_N \end{bmatrix}, \quad \mathrm{y} = \begin{bmatrix} -\left.\frac{\partial c}{\partial t}\right|_1 \\ -\left.\frac{\partial c}{\partial t}\right|_2 \\ \vdots \\ -\left.\frac{\partial c}{\partial t}\right|_N \end{bmatrix} \tag{3}$$

eq 2 can be expressed as

$$\mathbf{y} = X\mathbf{v} \tag{4}$$

Then, the estimated $\hat{\mathbf{v}}$ can be obtained using the least-squares method.[14]

$$\hat{\mathbf{v}} = (X^{\mathrm{T}}X)^{-1}X^{\mathrm{T}}\mathbf{y} \tag{5}$$

$\partial c/\partial x|_i$ and $\partial c/\partial y|_i$ are approximated using the difference between two sensor responses. It was found from the simulation that the direction of the gas flow was correctly obtained when the time constant of response recovery was less than the array size divided by the wind velocity.[13]

The important factor to obtain the clear image of the gas flow is the temporal resolution since it determines the maximum flow velocity that the system can follow. Although the response time of the semiconductor gas sensor is sufficiently short (<1 s), slow recovery (>30 s) was a serious problem. Thus, QCM (quartz crystal microbalance) gas sensors[15−19] were employed in the next version of the array.[20] Their faster recovery enabled the visualization of the gas flow up to 5 cm/s.

The temporal resolution of the system is determined not only by the recovery time of the sensors but also by the sampling rate of the sensor responses. The responses of QCM sensors are given in the form of frequency shifts. A multichannel reciprocal counter[21] is implemented in the system to achieve higher sampling rates of the sensor responses than the conventional frequency counter.[22] The sampling rate here was 8 samples/s, whereas it was 1 sample/s in the conventional frequency counter, i.e., binary modulus counter.

2.3.2.4. Experiment. The aim of the experiment here is to evaluate the capability of estimating gas-flow direction by a packed sensor array and to investigate the possibility of searching for an odor source by that array. The photo of sensor array and multichannel frequency countercircuit is shown in Figure 9. Twenty-one QCM gas sensors coated with sensing film (phosphatidylcholine) were mounted on the top board. In order to make a compact array, SMD (surface-mounted device)-type miniaturized AT-cut quartz resonators (27.8 MHz) were employed. Each sensor spans 4mm × 8 mm including an internally installed oscillator, and the distance between the sensors is 1.27 cm. On the bottom board, an FPGA (field-programmable gate array) chip was mounted. The 21-channel frequency shift measurement circuit was implemented into the FPGA.

The sensor responses along the wind direction are shown in Figure 10. The sensor array was placed 20 cm downstream from the source of triethylamine in the wind tunnel. Sensor 1 was at the upwind edge followed by successive sensors. The frequency shift of each sensor is normalized by the maximum value during the measurement. Since the timing for the sensors to reach their maximum values agrees with the sequence along the wind direction, the direction of the gas flow can be obtained. It should be noted that the conventional frequency counter with 1 sample/s cannot capture the difference in timing between sensors 1 and 5 because that difference is at most 1 s.

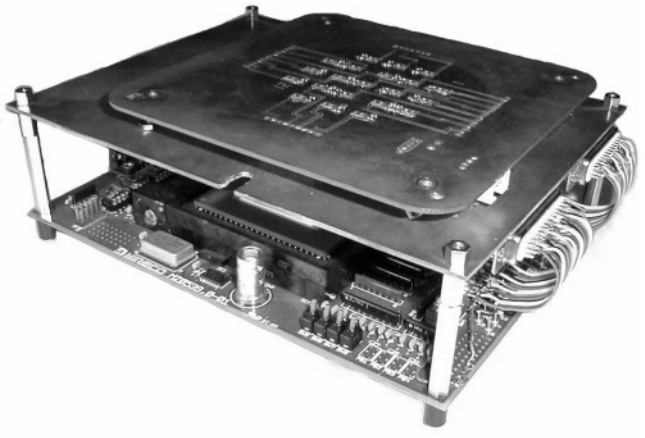

Figure 9. Photo of QCM gas sensor array and frequency counter circuit.

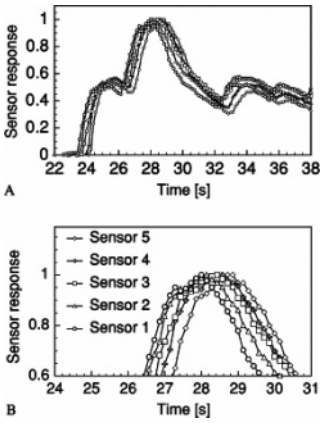

Figure 10. Response curves of 5 QCM sensors in a sensor array in a wind tunnel. Reprinted with permission from ref 22. Copyright 2002 Elsevier Science.

The sequence of visualized image in the wind tunnel is shown in Figure 11. The white pixel means that the sensor at that place has a large response, whereas the dark one has a small response. Four corners of the image are eliminated because no sensor is placed at those places. This figure reveals that the gas flows from left to right.

Figure 12 shows a histogram of the angular deviation of the estimated flow from the actual mean direction of the wind. The gas-flow direction can be estimated according to eq 5. The estimation was performed for 100 s. The deviation of the estimated directions in the range between −67° and −22°, one between −22.5° and 22.5°, and one between 22.5° and 67.5° are classified into −45°, 0°, and 45°, respectively. 74% of the estimated directions in Figure 12 are within the deviation of 67.5°. Although it may seem to be a large deviation, it is reasonable considering that the instantaneous wind direction itself was highly fluctuating. The deviation in Figure 12 is tolerable for plume tracking since the direction to track is repeatedly measured to approach the source.

Once the gas flow direction is obtained, the system can track it down to the source. An experiment was performed in the laboratory room to show the system's capability in source localization. A plastic bottle with a small hole on its

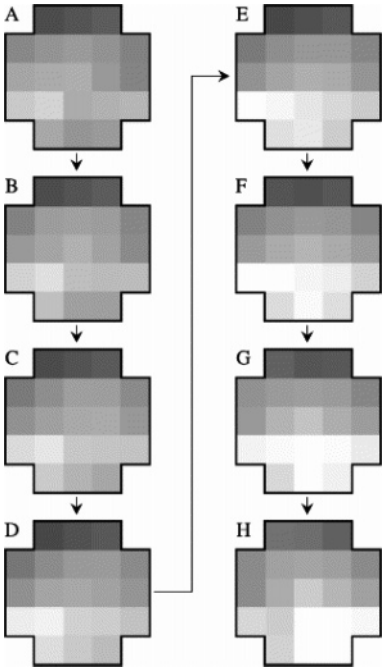

Figure 11. Sequence of visualized images in a wind tunnel. Reprinted with permission from ref 22. Copyright 2002 Elsevier Science.

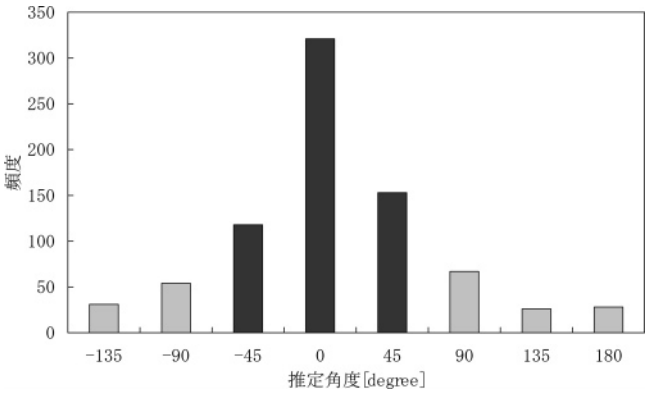

Figure 12. Histogram of errors in estimated direction obtained in wind tunnel.

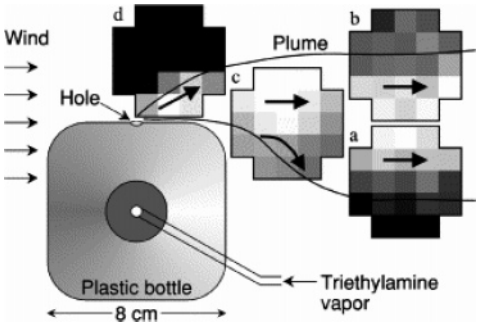

Figure 13. Visualized images around the gas leakage point. Thick arrows show direction of gas flows observed in visualized images. Reprinted with permission from ref 22. Copyright 2002 Elsevier Science.

side was prepared and the triethylamine vapor was leaked from that hole, as is shown in Figure 13.

The gas flowed from left to right at locations a and b. Then, the sensor array was placed at location c. Since the gas flow from left to right was observed at location c, the sensor array was moved to location d. The upper part of the image was dark, and the gas flowed from lower left to upper right. Thus, the gas leak position was localized. The plume-tracking technique based on single-point measurement cannot determine the source location until the field is thoroughly investigated for a long time.[23]

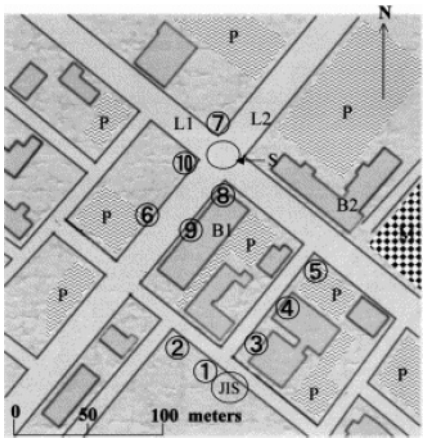

Figure 14. The locations of 10 NO_2 sensors in Sapporo, Japan. Reprinted with permission from ref 26. Copyright 2003 Elsevier Science.

The gas-flow imaging system enables the plume tracking even when the wind speed is too low to be detected using an anemometric sensor. This system is applicable to most of the situation where the wind speed is <30 cm/s. Thus, it can be used in ordinal domestic or industrial buildings.

2.3.3. Gas-Distribution Measurement by Sparse Sensor Array

2.3.3.1. Gas-Distribution Measurement for Monitoring Air Pollution. The packed two-dimensional sensor array is used to raise the estimation accuracy of the direction to the gas source within a short time. However, the sensor nodes are sparsely placed in a huge area when we monitor gas distribution in space. In this section, the measurement by a sparse sensor array is described.

In most of the cases, the gas distribution is measured to monitor air pollution such as NO_2, SPM, O_x, SO_2, and CO. Those are measured periodically by government stations, and the data are available from the web sites in almost real time[24,25] in Japan. However, the gas analyzer used in the station is very expensive, and the number of the stations is limited. Thus, the distance between the stations is long. The stations can be densely placed if cheap and reliable sensors are available.

Maruo and co-workers measured NO_2 distribution in Sapporo, Japan, using a porous glass substrate impregnated with a Saltzman reagent, an LED, and a photo detector.[26,27] The sensor element was a porous glass substrate with sulfanilamide (SFA) and *N*,*N*-dimethyl-1-naphthylamine (DMNA). A specific absorption peak appears at 525 nm, and the absorbance increases as exposure time or concentration increases. The interference from NO in the analysis of NO_2 was not significant. A photo detector received the light from a LED through the porous glass substrate. Its voltage was read by a microcomputer through an A/D (analog to digital) converter. The pump was not used because the wind blew constantly, and its performance was not influenced by the wind speed with the range between 0.5 and 5 m/s.

Those sensors were placed around the roadway intersection, as is shown in Figure 14. The measurement area is an

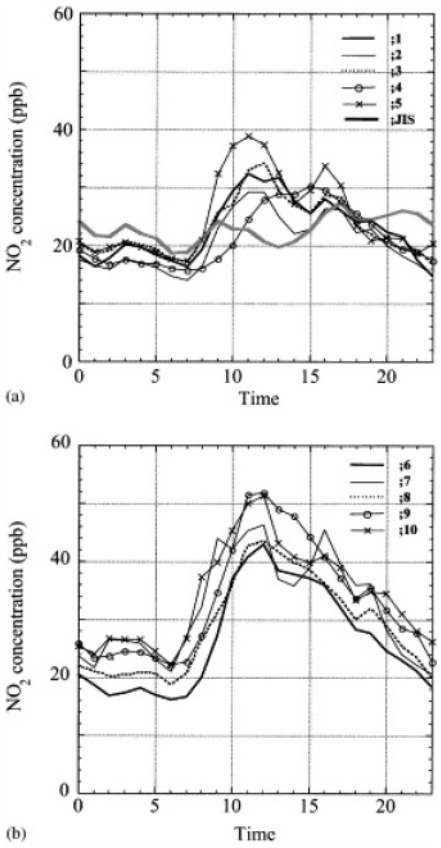

Figure 15. Measured NO_2 concentrations at all sites (July 2001). Reprinted with permission from ref 26. Copyright 2003 Elsevier Science.

inner-city area with two main roads of high traffic density (L1 and L2) and two tall buildings (B1 and B2), a large parking area (P), and markets (M). Approximately 24 000 vehicles pass these two main roads. They set a network composed of 10 sensor nodes to look at spatial and temporal variations of NO_2 concentrations every hour.

The measurement data during 24 h are shown in Figure 15. It shows the averages of 9 values from 9 different days. The typical pattern consists of a high level in the morning and in the evening and a low level during the night and in the afternoon. The proximity of road traffic increased NO_2 level. The small peak early in the morning was related to the peculiarity of this area where many trucks waited for the markets to open near the road early in the morning. At all the nodes 8, 9, 6, and 10 behind the tall building with southeast wind, the NO_2 level was low in the middle of night and the highest around noon. They said that the phenomenon of "street canyon" due to the tall buildings might occur. It was found that the concentration distribution was influenced by tall buildings and wind direction when they checked the wind direction.

Tsujita et al. reported the sensor network made up of semiconductor gas sensors to monitor NO_2.[28] The temperature and humidity sensors were also included in a sensor node to compensate for the sensor response. Moreover, a new autocalibration method was proposed to achieve maintenance-free operation for the sensor network. The lack of long-term stability is a serious problem of a gas sensor, which causes the deterioration of the measurement accuracy over time. Frequent recalibration is not realistic.

The network connectivity can be used not only for collecting the measurement data but also for the calibration

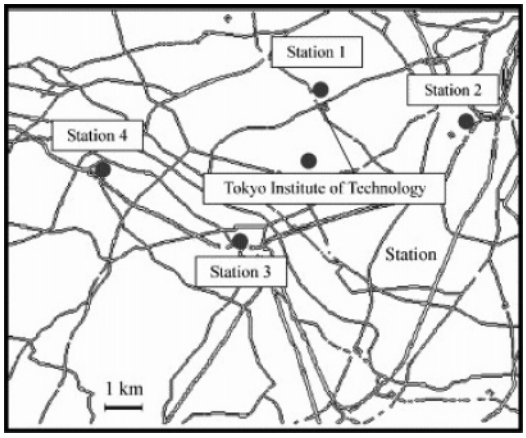

Figure 16. Monitoring stations around the measurement site. Reprinted with permission from ref 28. Copyright 2005 Elsevier Science.

and diagnosis of the sensors. The measured concentration can be easily compared through the network with those measured at nearby sensor nodes at government monitoring station. Although the different concentrations are usually monitored at different sites, the pollutant concentration in the whole local area becomes uniform in a certain weather condition. Each sensor in a network can be calibrated at that condition.

The case study was performed in the area shown in Figure 16. The semiconductor gas sensor and NO_x analyzer were placed at the university (Tokyo Institute of Technology). The four stations around that university were the government monitoring stations with gas analyzers. The hourly mean data measured at those stations are available at the web site.

The autocalibration procedure is as follows. In normal circumstances, NO_2 concentration in an urban area is high. In that case, the concentration within this local area is not uniform. However, it would be reasonable to consider that the concentration at the monitoring site is almost zero when the concentrations of all the stations around the monitoring site were near zero. This unusual low concentration might be obtained due to small traffic on a national holiday or extremely large dilution of NO_2 in a stormy day. The gas sensor output around the baseline can be calibrated on this special case by assuming the uniformity of the concentration. A sensor at a node connected to a network is automatically calibrated using this assumption.

The raw sensor data and the data reported at the environmental monitoring stations were collected for several months. The initial calibration of the gas sensor was performed immediately before starting the long-term measurement. Two months after the gas sensor was calibrated, the measurement error increased to ~40 ppb. Figure 17 includes the occasion when the calibration was performed. Dashed line shows that calibrated sensor value after adjusting the sensor baseline at 1445 h to the average of the concentrations reported from surrounding stations. The sensor output after the baseline adjustment agreed well with NO_2 concentration obtained from NO_x analyzer. This autocalibration method was effective to maintain the accuracy of the sensor system in an atmospheric-monitoring network.

Another point of view in a sensor placed in the ambient air is a vapor-sampling method. In the case of a packed sensor array, sensors are directly exposed to the ambient air. On the other hand, the air is sometimes sucked by a pump at each sensor node in the case of a sparse sensor array.

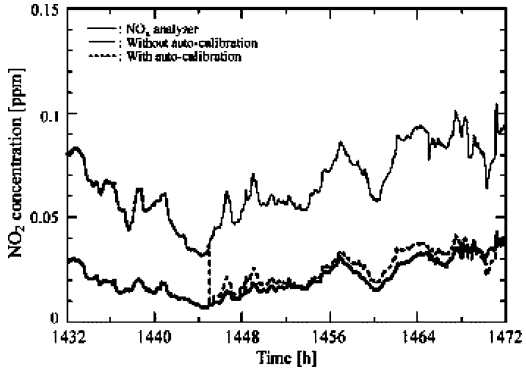

Figure 17. Comparison of NO_2 concentration with gas sensor and NO_x analyzer when autocalibration was performed. Reprinted with permission from ref 28. Copyright 2005 Elsevier Science.

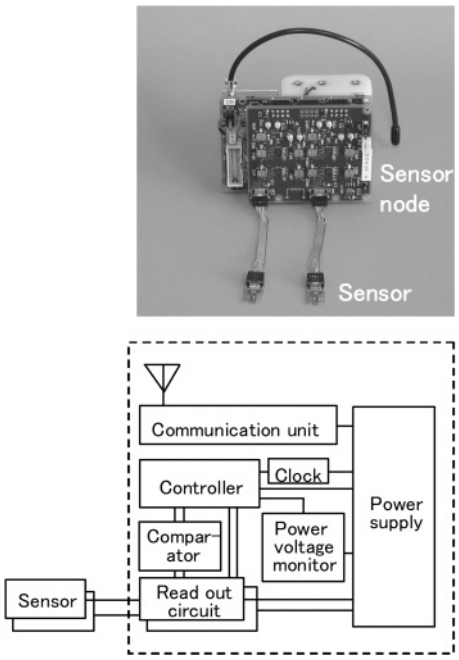

Figure 18. Photo and block diagram of sensor node for hydrogen detection. Reprinted with permission from ref 31. Copyright 2005 IEE of Japan.

However, sampling schemes for sensors to detect vapors are important. Settles reviewed the fluid dynamics about sniffers for the point-detection devices.[29] It was also reported that the vapor discrimination capability was enhanced when a sensor chamber mimicking a nasal cavity was used.[30]

2.3.3.2. Gas-Distribution Measurement for Monitoring Hydrogen Leak. Gas distribution is also measured to check the leakage of combustible or toxic gases. Gas distribution should be monitored real time to localize the leakage location. A wireless network for detecting hydrogen leak was proposed.[31] Hydrogen filling stations are expected to become common in the near future when fuel-cell cars are widely used. Thus, a sophisticated hydrogen monitoring system is required. The employed sensor is a FET (field effect transistor) gas sensor[32] with a catalytic metal gate (Pd), which works at 100 °C. Heating the sensor reduced the humidity influence and the response time.

They constructed a prototype sensor network to detect hydrogen using 10 sensor nodes. A photograph and block diagram of a sensor node is shown in Figure 18. Each sensor node has two sensors, a readout circuit, a controller, a communication unit, and a power supply. The controller includes a microcomputer with low power consumption and short rise time from standby mode to active mode. The communication unit sends and receives signals at 430 MHz. The communication area was wide enough to cover a hydrogen filling station (at least 100 m^2). The function of reducing the power was implemented. Initially, the sensors worked at room temperature without heating. Once the sensor signal exceeded the threshold, the microcomputer woke up to change from standby mode to active mode. Then, it switched the heaters attached to sensors. Each sensor node consumed much power only when hydrogen was detected. Testing showed that the signal came to the access point within 0.3 s after the sensor was exposed to hydrogen.

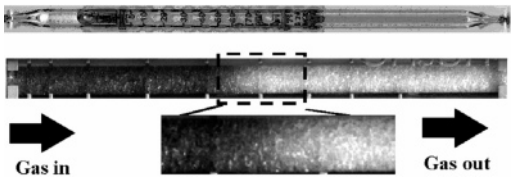

Figure 19. Discoloration of gas detector tube exposed to methyl mercaptan.

2.3.3.3. Bad-Smell Sensing Network. The final topic in this subsection is a bad-smell sensing network composed of gas-detector tubes. Recently, the deterioration of the environment caused by bad smell has become one of the problems in daily life. Although the gas chromatograph/mass spectrometry (GC/MS) method is often used to analyze gases, it is time-consuming. Moreover, it is impossible to do the onsite monitoring when GC/MS is used. Gas-detector tubes were used here since they are cheap and easily handled.[33]

In the gas-detector tube, the fundamental function of the chemical reaction between the analyte and the reagent system is to form color compounds that make the reaction visible.[34] A gas concentration is visually obtained by reading the length affected by the color change. Although the discoloration-layer length has been manually read, the optical sensor enables the automatic measurement of the gas detector tube. The automatic measurement increases the accuracy and the reproducibility of the measured data. Moreover, the sensitivity is enhanced by the continuous gas sampling and capturing the image of the gas-detector tube because of the accumulation effect. Three types of image sensors such as A4-size optical scanner,[35] one-dimensional CCD sensor,[36] and mobile phone camera[37] were utilized to capture the image of the gas-detector tube. When each sensor system is equipped with a communication module, the sensing network is realized. The bad-smell sensing network was constructed and was applied to the measurement at the paint factory.[38]

The photo of the gas-detector tube (Gastec, No. 71) is shown in Figure 19. When methyl mercaptan vapor was flowed to the gas-detector tube, its color changed from white to yellow. The selectivity of the gas-detector tube is larger than that of typical gas sensor, and a few hundreds kinds of gas-detector tubes are commercially available. The disadvantage of the gas-detector tube is its irreversible reaction. Once the discoloration occurs along the whole length, it cannot be used again.

Since the brightness change along the detector tube axis is not smooth, the noise reduction technique was applied to the image of the gas-detector tube.[35] Using the method in ref 35, the discoloration-layer length was obtained. The result is shown in Figure 20 when several temporal changes of gas concentrations were tried. The gas was supplied from

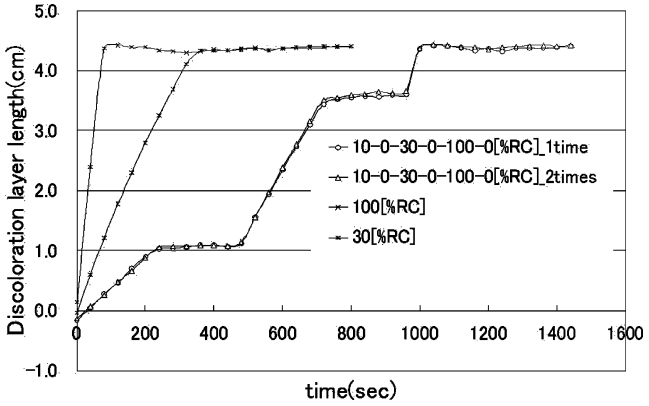

Figure 20. Temporal change of discoloration-layer length under several gas concentration profile (methyl mercaptan). Reprinted with permission from ref 35. Copyright 2004 IEE of Japan.

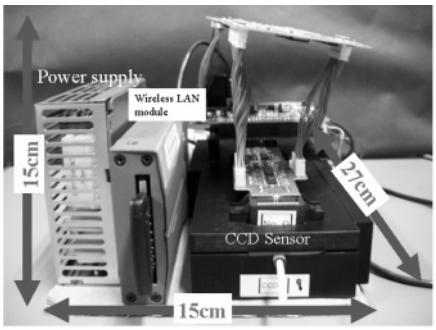

Figure 21. Photo of gas detector tube system combined with one-dimensional CCD image sensor.

the blender based upon high-speed switching of a solenoid valve.[39] The concentration was a relative one with the unit [% RC]. 100 [% RC] was the maximum concentration and corresponded to 2−2.5 ppm.

The two curves in the left portion correspond to concentrations 100 and 30 [% RC]. It was found that the slope of the curve became larger when the concentration became higher. The two curves in the right portion were obtained when the vapor with the concentrations 10, 0, 30, 0, 100, 0 [% RC] was exposed for each corresponding 4 min. The reproducibility was good because the two curves with the same concentration profiles were almost overlapped. Moreover, the discoloration stopped when the tube was exposed to air at 0 [% RC]. The discoloration stopped at 4.5 cm because that point is the edge of the reagent region.

A photo of the gas-detector tube system combined with a one-dimensional CCD sensor is shown in Figure 21. It includes a one-dimensional CCD, LEDs for illumination, a microcomputer, and wireless LAN (local area network) modules. The gas-detector tube was put into the black acrylic box to prevent influence of the light from the outside. Using this system, the gas (methyl mercaptan) with low concentration (30 ppb) was measured as is shown in Figure 22. The accuracy of measuring the length of the discoloration layer was much better than that of typically used manual inspection because it was difficult to check the brightness change within the region of 1 mm by manual inspection. However, a tiny change of the discoloration layer was clearly captured by the CCD image sensor. The sensitivity was improved by 1 order of magnitude compared with the manual inspection.

Since this system has the function of communication, the data from the multiple sensor nodes can be collected through the wireless LAN. The six sensor nodes were placed at the

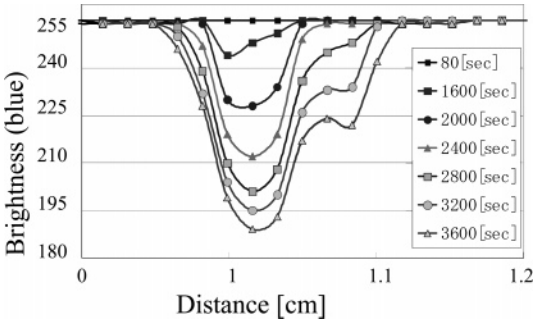

Figure 22. Brightness distribution along axis of gas detector tube for 30 ppb methyl mercaptan. Reprinted with permission from ref 36. Copyright 2006 Elsevier Science.

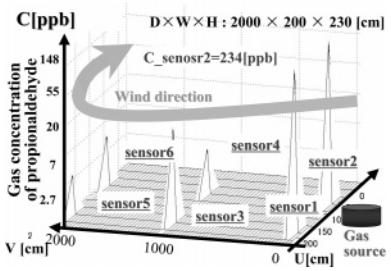

Figure 23. Result of gas distribution measurement at corridor using bad-smell sensing network composed of gas detector tubes.

corridor of the building. The measurement area was 2 m × 20 m, and the sample was propion aldehyde. Sensor nodes 5 and 6 were 20 m away from the source, and those nodes were placed outside the building. The petri dish filled with the liquid of propion aldehyde was placed at the corridor, and the concentration just above the petri dish was 18 ppm.

Figure 23 shows the gas distribution obtained from six sensor nodes. The gas-detector tube responded to the vapor at the place even 20 m away from the source. Although the highest concentration was measured at sensor node 2, it was ∼200 ppb. The response at node 4 was higher than that at node 3, whereas the response at node 6 was higher than that at node 5. This phenomenon might be caused by the change of the wind direction along the corridor, as is illustrated in Figure 23. This result indicates that it is possible to do the field measurement using a bad-smell sensing network composed of gas-detector tubes.

Although the image of a single gas-detector tube is captured using a one-dimensional CCD sensor, the image of multiple gas-detector tubes can be simultaneously captured when two-dimensional image sensor is employed. Moreover, it is better to collect the data even when the sensor nodes are far away from each other. Thus, the mobile phone camera was used because of its communication capability. The photo of the sensor node using the mobile phone camera is shown in Figure 24. The light source and the multiple gas-detector tubes were placed inside the black acrylic box. The mobile phone camera was placed at the top of the acrylic box. It was controlled by a microcomputer, and the image was periodically captured. The measurement can be automatically performed. The concept of a bad-smell sensing network using a gas-detector tube and a mobile phone camera is illustrated in Figure 25. Each sensor node sends the host computer the image file attached to the e-mail. The host computer collects the image files from many nodes, and the gas distribution is obtained after the analysis. Using this system, it is possible to collect the data from many sensor nodes located far away from each other.

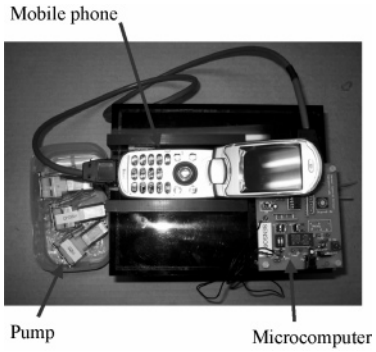

Figure 24. Photo of sensor node using mobile phone camera. Reprinted with permission from ref 37. Copyright 2007 Elsevier Science.

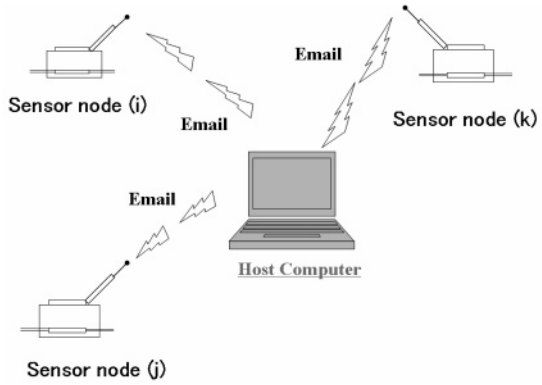

Figure 25. Concept of bad-smell sensing network using gas detector tube and mobile phone camera.

2.3.4. Measurement of Continuous Distribution of Gas Using Optical Method

2.3.4.1. Backscatter Gas Absorption Imaging. Backscatter absorption gas imaging (BAGI) is a technique to realize the real-time visualization of gas plume using laser-based remote sensing.[40] A field is illuminated by a narrow-bandwidth infrared laser. Gas visualization occurs if a plume absorbing the laser radiation is located in that field. Its presence causes a dark plume image in the video picture.

The description of the long-range BAGI imager is summarized here.[41] The imager operates in a raster-scanned mode to achieve real-time laser-illuminated imaging at a wavelength between 9 and 11 μm tuning range of the CO_2 laser. Scanning of both the 18 W continuous-wave CO_2 laser beam and the instantaneous field-of-view of the single-element detector is accomplished using a pair of galvanometrically driven mirrors.

The imager viewed the release of sulfur hexafluoride gas at the range of 90 m in the test field. Figure 26 shows BAGI images under condition of no gas, 3 ppm SF_6, and 40 ppm SF_6. The dark plume images were observed when SF_6 gas was present.

There are a few aspects to be considered when BAGI images are observed. First, gas imaging requires a hard target in the imager field-of-view. In the case of Figure 26, a 12 ft^2 panel was placed to serve as a backscattering surface. Second, BAGI requires the spatial contrast in gas concentration. It is not possible to detect uniformly distributed gases. Third, BAGI has a large signal-to-noise ratio compared with the passive gas visualization method because of active laser illumination.

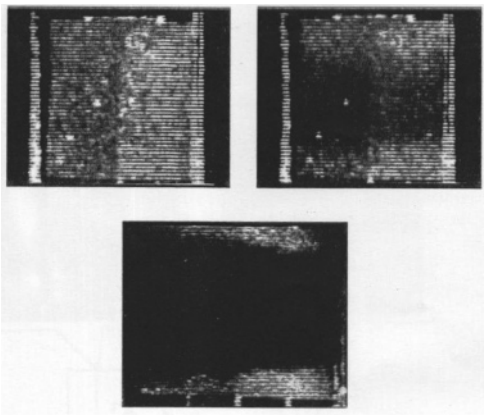

Figure 26. BAGI plume image taken at a range of 90 m. Top left image is taken at no gas release. Top right image is taken with 3 ppm SF_6 release; lower image is taken with 40 ppm SF_6 release. Reprinted with permission from ref 41. Copyright 1997 SPIE.

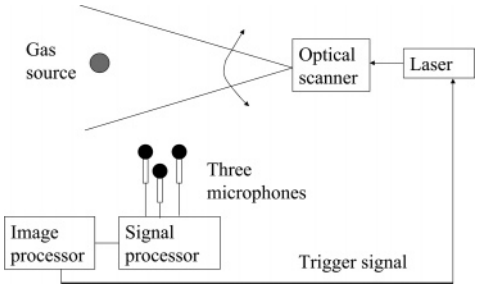

Figure 27. Experimental setup for gas-distribution measurement using photoacoustic effect.

Another approach employed the differential absorption mode.[42] In this mode, two wavelengths, where the light energy is absorbed and not absorbed by the gas to be detected, are used, respectively. Images are displayed as the natural logarithm of the ratio of the on wavelength absorbed by the gas to the off wavelength not absorbed by the gas. Using this technique, the topographic scene image is removed, whereas the plume image is displayed. Thus, an optical method can be used to obtain a gas plume image.

Nagashima et al. proposed the wavelength-differential image obtained by subtracting two images through the variable interferometer with different transmission spectra. They observed the plume of butane using this method.[43]

2.3.4.2. Measurement of Gas Distribution Using Photoacoustic Effect. This method is a combination of an optical method with an acoustic one. Ochiai et al. studied the measurement system of the gas distribution using photoacoustic effect.[44] The experimental setup is illustrated in Figure 27. Adsorption of light at a certain wavelength occurs because of the existence of gas. The absorbed energy is converted to heat, followed by expansion. When the light illumination is periodically performed, the expansion and contraction occur synchronously with light illumination. Then, the sound is generated. The laser beam is two-dimensionally scanned. The generated sound is detected by three microphones placed three-dimensionally. The method of localizing a sound source can be used to determine the location of the gas source. Ochiai et al. applied this method to the localization of methane source. This method is fascinating because the gas source can be replaced with a sound source and the problem of the sound-source localization in place of the gas-source one is solved.

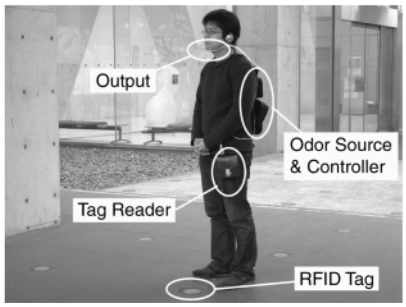

Figure 28. Odor field presentation system. Reprinted with permission from ref 45. Copyright 2006 IEEE.

2.4. Presentation of Virtual Odor Source

Recently, several researchers were interested in forming the odor plume in a virtual environment.[45] People can perceive the object with smell in that environment. In virtual reality, an olfactory display to present smells is focused on.[46] The direction to an odor source, the feeling of approaching or going away from it, may be realized even if the actual odor source is not in front of people. Thus, one of the research studies about an olfactory display is to localize an odor source in a virtual environment.

Yamada et al. proposed the wearable olfactory display as is shown in Figure 28. The wearable olfactory display is equipped with a man in the photo. The gas concentration can be controlled using this system, and a tag reader and a radio frequency identification (RFID) tag were used to determine his position. The smell flowed from the slit in the adaptor indicated as the output in this figure. The intensity of the presented odor was controlled by changing the ratio of the air flow rate to that of the odor flow rate. The flow was driven by a DC motor air pump. By changing the concentration of the gas presented from a wearable olfactory display according to the position obtained from the tag reader, a gas field model in a wide space was realized in a virtual environment. When a subject approached the virtual odor source, the intensity of the odor from the slit increased. On the other hand, the odor intensity decreased as the subject was away from the virtual odor source.

The gas field model employed here is an isotropic solution, assuming that the diffusion equation without air stream is valid. Although this assumption is not valid in the actual case because gas molecules are mainly carried by the air flow, they used this gas field for the first step to realize the virtual olfactory environment.

Several subjects tried to find the virtual odor source within the area 18 m × 9 m. Tracking behaviors of the odor source and temporal changes of gas concentrations are shown in Figure 29. From that figure, both subjects reached the vicinity of the odor source by trial and error, changing their directions on the basis of the sensation of changing odor. They said that the subjects could perceive spatial information of odor presented by the wearable olfactory display. The subjects took two ways to explore the virtual odor source. Subject C chose the strongest point of odor after searching through the entire region. On the other hand, subject D walked randomly and changed the direction so that a stronger perception of the odor could be obtained.

This is a very simple case of the presentation of the virtual odor source. In the actual situation, the odor plume is governed by the wind. This behavior is obtained by solving the Navier−Stokes equation. This is the fluid dynamics problem to be solved using a finite-element method, and it consumes much time to obtain the exact three-dimensional solution. The tradeoff between the time and the accuracy should be examined when the odor source in the virtual environment is studied.

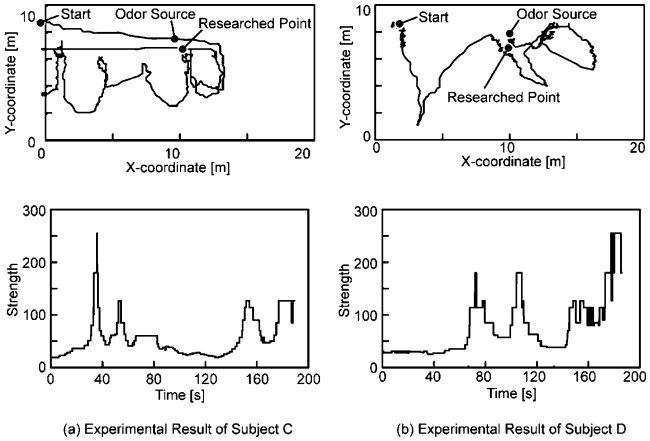

Figure 29. Behavior of tracking virtual odor source and temporal concentration change according to subject's position. Reprinted with permission from ref 45. Copyright 2006 IEEE.

3. Analysis of Temporal Response

In addition to the traditional static method, the dynamic behavior of the gas sensor offers useful information of odor identification. First, the sensor dynamics model and its analysis method are described. Especially, the methods of extracting time constants based on the diffusion model and the autoregressive (AR) model are presented. The application of the system-identification model to the analysis of the gas sensor is also explained. The frequency analysis is often useful for extracting the features from the temporal data. It is also described here. Finally, the temporal-data analysis of the preconcentrator with variable temperature with its interesting feature is shown. Thus, the analysis of the sensor dynamics is reviewed in this section.

3.1. Analysis of Sensor Dynamics

It is required to obtain both input and output signals when we determine the model of sensor dynamics. However, it is not always possible to know input signal, i.e., the temporal change of vapor concentration. Thus, a certain situation should be considered to know the input signal.

The simplest method to analyze the dynamic behavior is to obtain the step response of the gas sensor.[47] They reported that the model parameters derived by fitting the model to the experimental data of the step response represented the type of the gas and its concentration. However, the gas concentration change should be much faster than the time constant of the gas sensor. Moreover, the concentration should be kept constant after the beginning of the vapor exposure.

The second method is to obtain the impulse response of a gas sensor.[48] When we use the simple vapor supply system as is shown in Figure 30, it is very difficult to keep the concentration constant during the vapor exposure. The air is flowed from the sample bottle, and the vapor at the headspace over the liquid is carried to the sensor. Although the concentration is high at first, it gradually decreases during the vapor exposure because the flow rate typically exceeds the evaporation rate of the sample. Since this dynamics is

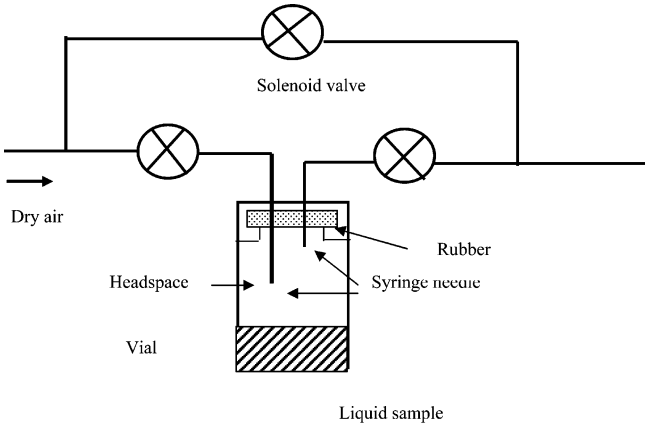

Figure 30. Simple method of supplying headspace vapor.

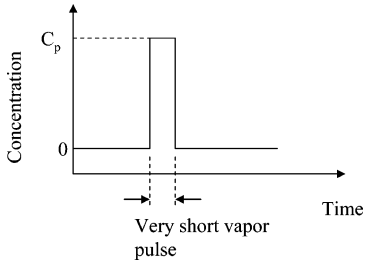

Figure 31. Vapor concentration change in pulse vapor supply method.

complicated, it is not easy to model the concentration change at the outlet. Thus, the sensor was exposed to a very short vapor pulse, as is illustrated in Figure 31. The concentration change at the sample bottle can be ignored if the vapor pulse is much shorter than the time constant of the sensor. Although the same vapor supply method was used, the time for vapor exposure is very short: just 1 s. In this situation, we do not have to know the input signal, i.e., vapor concentration.

In the third method, the vapor concentration at the sensor is allowed to be dynamically changed. In this case, it is required to know the vapor concentration change at the sensor precisely. One of the methods is to use a sensor with a very fast response.[49] Although that sensor has a time constant of a few milliseconds, the gas species to be detected are limited. Thus, the visualization method of the gas flow using an optical tracer described in earlier section was used.

In this approach, an optical tracer is effective to obtain the instantaneous vapor concentration at a sensor using the gas-distribution visualized system shown in Figure 3. The brightness change at the CCD camera was measured simultaneously with the tin oxide gas sensor response to the sample vapor from the joss stick, as is shown in Figure 32. The gas sensor (TGS800, Figaro) was placed just below the light sheet, and the mean brightness within 10 × 10 pixels over the area of the gas sensor was obtained. The sampling intervals of gas sensor response and brightness were 0.1 and 0.04 s, respectively. The gas concentration changes very rapidly in the figure since the plume was meandering, as is shown in Figure 4. Therefore, the brightness calculated from the image fluctuated rapidly and resulted in the irregular train of pulses, considerably different from the gas sensor response. A similar phenomenon was observed elsewhere.[50] The response and recovery speeds of the gas sensor are not enough to catch up with the concentration pulses in Figure 32. These concentration pulses can be used as input signals of a sensor response model described in the next subsection.

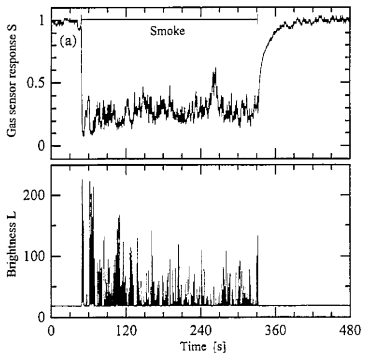

Figure 32. Sensor response measured simultaneously with gas concentration obtained using optical tracer. Reprinted with permission from ref 6. Copyright 1998 Elsevier Science.

In this subsection, three approaches based upon step response, impulse response, and irregular change of the vapor concentration were described. If the linear superposition theorem is valid, the impulse response approach is useful because just the simple vapor supply method is sufficient. However, the final approach should be taken if the nonlinear property is dominant.

3.2. Sensor Dynamics Model When Instantaneous Gas Concentration Is Available

There are several sensor dynamics models.[51,52] The simplest model is a linear one governed by the equation below.

$$\frac{d^n y(t)}{dt^n} + a_1 \frac{d^{n-1} y(t)}{dt^{n-1}} + \cdots + a_{n-1} \frac{dy(t)}{dt} + a_n y(t) = b_0 \frac{d^m u(t)}{dt^m} + b_1 \frac{d_{m-1} u(t)}{dt^{m-1}} + \cdots + b_{m-1} \frac{du(t)}{dt} + b_m u(t) \quad (n \geq m) \quad (6)$$

where $y(t)$ is a sensor response, $u(t)$ is the gas concentration, and a_i and b_i are the coefficients. Laplace transform is performed by

$$Y(s) = \int_0^\infty y(t)\, e^{-st}\, dt \quad (7)$$

In the form of Laplace transform, the transfer function $G(s)$ is

$$G(s) = \frac{b_0 s^m + b_1 s^{m-1} + \cdots + b_m}{s^n + a_1 s^{n-1} \cdots a_{n-1} s + a_n} \quad (8)$$

When this model was applied to the response of the semiconductor gas sensor as is shown in Figure 32, a second-order differential equation

$$\frac{d^2 y(t)}{dt^2} + \alpha_i \frac{dy(t)}{dt} + \beta_i y(t) = g_i l_s(t) \quad (9)$$

is assumed, where $l_s(t)$ corresponds to the steady-state response to the vapor with the concentration at time t. $l_s(t)$ can be in advance obtained from the calibration curve.

α_i, β_i, and g_i are the coefficients. In the case of the semiconductor gas sensor, the rise time of the response is much shorter than the recovery one. Thus, the waveform is divided into two phases such as response and recovery

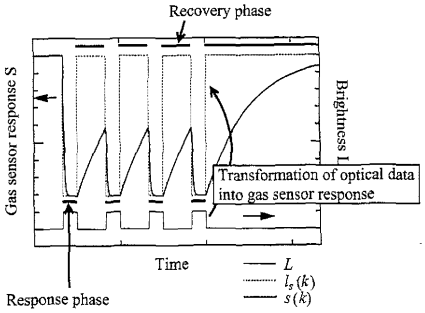

Figure 33. Scheme for dividing a waveform into two phases such as response and recovery phases. Reprinted with permission from ref 6. Copyright 1998 Elsevier Science.

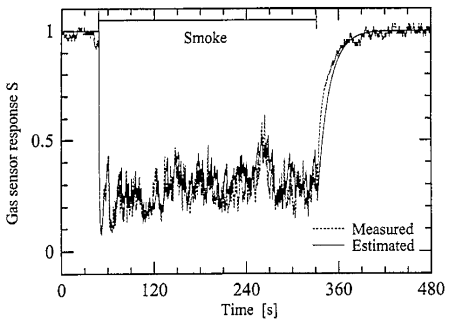

Figure 34. Comparison of estimated semiconductor gas sensor response with measured one when optical tracer and second-order model were used. Reprinted with permission from ref 6. Copyright 1998 Elsevier Science.

phases, as is illustrated in Figure 33. In eq 9, i is equal to 1 for the response phase, whereas it is 2 for the recovery phase.

Equation 9 is transformed into the discrete form

$$y(k+1) = p_i y(k) + q_i y(k-1) + r_i l_s(k) \qquad (10)$$

where $y(k)$ = gas sensor response at time $k\Delta t$; $l_s(k)$ = transformed steady-state sensor response corresponding to the brightness at time $k\Delta t$; Δt = sampling interval (0.1 s); p_i, q_i, and r_i = constants; $i = 1$, response phase; and $i = 2$, recovery phase.

If $l_s(k) < y(k)$, $y(k)$ is in the response phase, whereas it is in the recovery phase if $l_s(k) > y(k)$. The parameters p_i, q_i, and r_i in eq 10 were estimated for the response phase and the recovery one, respectively. Comparison of the estimated response with the measured one is shown in Figure 34. The estimated gas sensor response agreed well with the experimental one.

The model above is effective when we use a slow-speed gas sensor. However, it is not sufficient for a faster-speed gas sensor since the switching between the response and recovery phases is too frequent. The deviation was larger when a QCM (quartz crystal microbalance) gas sensor was used. Thus, another approach is to construct a model using a neural network.[53] When we use a neural network, it is not necessary to divide waveform into response and recovery phases because it is a nonlinear technique. A neural network employed here was a MLP (multilayer perceptron) trained with error back-propagation algorithm.[54,55] It is possible to realize any continuous function from input to output using a three-layer network, given a sufficient number of hidden units, proper nonlinearities, and weights.[56] Thus, a neural network illustrated in Figure 35 was used. The sensor response at $k + 1$ is obtained using $l_s(k + 1)$, $l_s(k)$, $y(k)$, and $y(k - 1)$, as is illustrated in Figure 35a. The output of the

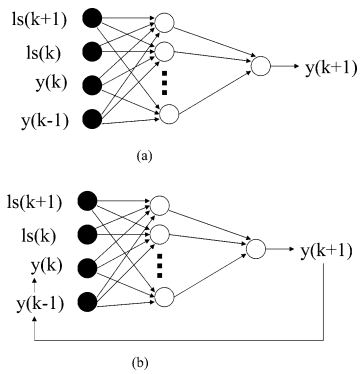

Figure 35. Structure of MLP (a) in the training and (b) in the estimation when transient gas sensor response is estimated using an optical tracer.

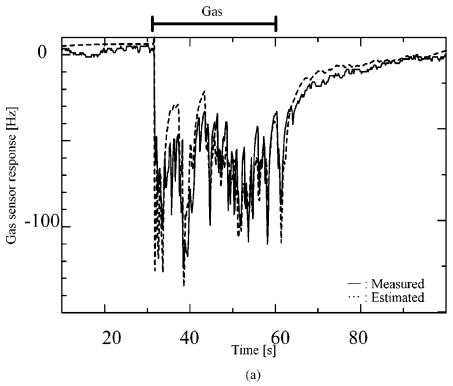

Figure 36. Comparison of estimated QCM gas sensor response with measured one when optical tracer and MLP model were used. Reprinted with permission from ref 7. Copyright 2002 IEICE of Japan.

neural network, i.e., the estimated sensor response, is fed back to the input layer when the estimation is performed, as is illustrated in Figure 35b.

The experimental result is shown in Figure 36. The QCM gas sensor (29.5 MHz, AT-cut) coated with a sensing film, phosphatidylcholine, was exposed to triethylamine vapor, and a tiny hollow polymer sphere was used as an optical tracer. The sensor data were sampled every 170 ms using a reciprocal counter.[21] The numbers of input, hidden, and output layer neurons were 4, 20, and 1, respectively. It was found that the estimated sensor response agreed well with the experimental one even when the sensor with the speed faster than that of the semiconductor gas sensor was used.

3.3. Extraction of Time Constant

3.3.1. Diffusion Model and Its Modification

An odor-sensing device often called an electronic nose consists of a sensor array and a pattern-recognition technique. The output pattern of a sensor array with partially overlapping specificities is recognized by a neural network or multivariate analysis. Although there are a variety of gas sensors such as semiconductor gas sensors,[57−62] QCM gas sensors,[63−72] SAW (surface acoustic wave) gas sensors,[73−77] cantilever-type gas sensors,[78,79] FPW (flexural plate wave) gas sensors,[80] conducting polymer gas sensors,[81−84] carbon black polymer gas sensors,[85−87] MOS (metal oxide semiconductor) gas sensors,[88−90] MS (mass spectrometry),[91−93] IMS (ion mobility spectrometry)[94] high-speed gas chromatographs,[95] optical gas sensors,[96−99] and electrochemical gas sensors,[100] more in-

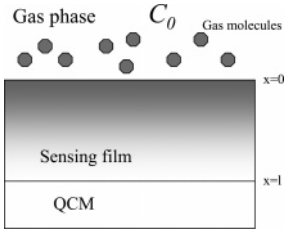

Figure 37. Gas sorption at sensing film of QCM gas sensor.

formation is required to achieve reliable discrimination. Thus, time constant as well as amplitude information has been studied to use an element of a pattern vector.

When we obtain the time constant, a sensor-response model is required. First, the sensor-response model based upon the diffusion model is described. When a QCM gas sensor was considered, vapor diffused into a coating film, as is illustrated in Figure 37. Gas molecules diffuse into a sensing film with the thickness l according to Fick's law.[101] The concentration in the sensing film $c(t,x)$ is governed by

$$\frac{\partial c(t,x)}{\partial t} = D\frac{\partial^2 c(t,x)}{\partial x^2} \tag{11}$$

under the boundary conditions

$$c(0,x) = 0$$
$$c(t,0) = C_0$$
$$\left.\frac{\partial c}{\partial t}\right|_{x=l} = 0 \tag{12}$$

where C_0 is the concentration in the gas phase. Solving eq 11 under the boundary conditions above,

$$c(t,x) = C_0 - \sum_{n=1}^{\infty}\frac{4C_0}{(2n-1)\pi}\exp\left(\left(-\frac{2n-1}{2l}\pi\right)2Dt\right)\sin\frac{2n-1}{2l}\pi x \tag{13}$$

is obtained, assuming the diffusion coefficient D is not dependent on $c(t,x)$, the concentration inside the sensing film. The amount of sorption $y_s(t)$ is

$$y_s(t) = \int_0^l c(t,x)\,\mathrm{d}x = C_0 l\left(1 - \sum_{n=1}^{\infty}\frac{8}{(2n-1)^2\pi^2}\exp\left(-\left(\frac{2n-1}{2l}\pi\right)^2 Dt\right)\right) \tag{14}$$

At equilibrium,

$$y_s(\infty) = C_0 l \tag{15}$$

Thus,

$$\frac{y_s(t)}{y_s(\infty)} = 1 - \sum_{n=1}^{\infty}\frac{8}{(2n-1)^2\pi^2}\exp\left(-\left(\frac{2n-1}{2l}\pi\right)^2 Dt\right) \tag{16}$$

is obtained.

When the diffusion governs the vapor sorption onto the sensing film, the experimental data fits well to the curve of eq 16. However, the curve fitting was sometimes unsuccessful. Not only the diffusion but also the surface adsorption should be taken into account. Thus,

$$y_s(t) = y_{s1}\left[1 - \sum_{n=1}^{\infty}\frac{8}{(2n-1)^2\pi^2}\exp\left(-\left(\frac{2n-1}{2l}\pi\right)^2 Dt\right)\right] + m_1\left(1 - \exp\left(-\frac{t}{\tau_1}\right)\right) \tag{17}$$

can be used for the curve fitting where m_1 and τ_1 are the amount of adsorption and its time constant, respectively, assuming that the speed of the surface adsorption is much faster than that of diffusion. Practically, the term without $n = 1$ can be ignored in most cases. Then, the simple equation using two time constants

$$y_s(t) = m_1\left(1 - \exp\left(-\frac{t}{\tau_1}\right)\right) + m_2\left(1 - \exp\left(-\frac{t}{\tau_2}\right)\right) \tag{18}$$

can be used for the curve fitting of a QCM gas sensor.[101] Moreover, the time constant in the response phase is different from that in the recovery phase in the same manner as that of the semiconductor gas sensor in the previous section. Since the time constant in the recovery phase is longer than that in the response phase, it is easier to analyze the waveform during the desorption so that many data points can be used for the curve fitting.

3.3.2. AR Model

In contrast to the method above, the AR (autoregressive) model is also effective to determine the time constant.[102] The AR model is typically used to estimate parameters in a dynamic system. It is assumed that $y_s(k)$ satisfies the AR model

$$y_s(k) + \sum_{i=1}^{L}\alpha_i y_s(k-i) = e(k) \tag{19}$$

where L is the order of the model, $e(k)$ is the residual error, and α_i is the scalar coefficient. By solving the equations

$$\frac{\partial}{\partial\alpha_i}\sum_k e^2(k) = 0 \tag{20}$$

the optimal α_i can be obtained. Assuming that $y_s(k)$ is the sum of L exponentials,

$$y_s(k) = \sum_{i=1}^{L} b_i r_i^{\,k}, \quad r_i = \exp(-\Delta t/\tau_i) \tag{21}$$

is obtained where τ_i is the time constant and b_i is the scalar coefficient. The Z-transform of eq 21 is

$$Z[y_s(k)] = \sum_{i=1}^{L}\frac{b_i}{1 - r_i z^{-1}} = \frac{B(z^{-1})}{A(z^{-1})} \tag{22}$$

The denominator of $Z[y_s(k)]$ is

$$A(z^{-1}) = (1 - r_1/z)(1 - r_2/z)\cdots(1 - r_L/z) \tag{23}$$

On the other hand,

$$Z[y_s(k)] + \sum_{i=1}^{L} \alpha_i z^{-i} Z[y_s(k)] = Z[e(k)] \qquad (24)$$

using eq 19. Then,

$$Z[y_s(k)] = \frac{Z[e(k)]}{1 + \sum_{i=1}^{L} \alpha_i z^{-i}} \qquad (25)$$

Using eqs 22, 23, and 25, it is found that r_i is the solution of $A(z^{-1}) = 0$.

Thereafter, the time constant τ_i is obtained. Nakamura et al. applied this method to the step response of a QCM gas sensor and obtained the time constants with high accuracy.[102] Using this method, the time constants of acetone, 2-butanone, methanol, ethanol, benzene, and toluene were obtained. The PCA (principal component analysis) result of the steady-state responses of six sensors and those of time constants are shown in parts a and b of Figure 38. It was found that the separation among samples became clear when the time constant information was included. They also proposed the method using linear filter and plural sensors even when the gas concentration was changed.[103]

3.3.3. System Identification Model

The effort to build a mathematical model of a gas sensor as a dynamical system has been done from the viewpoint of system identification. Here, the attempt to model the sensor response to the gas mixture is described. The gas sensor is modeled as a MISO (multi-input single-output) system.[104] When the nonlinearity is included, the three methods such as functional expansions, block-structured network model, and neural network were proposed.

Functional expansions are valid representations of nonlinear systems under assumptions (stationarity). In the case of a nonlinear time-invariant system, the transfer function can be expressed as a Volterra functional expansion which includes n kernels.

The block-structured model consists of interconnections of two different classes of blocks such as dynamic linear blocks and static nonlinear blocks. Figure 39 shows several possible typical topologies for modeling the sensor response to a binary mixture.[105,106] These models are easier to implement compared with the kernel representation.

Another method is the neural network. The neural network can model a highly nonlinear relationship if there is enough hidden-layer neurons. Time-delayed and recurrent-type neural networks were used to obtain the concentration changes of the binary mixture (octane and toluene).[107]

Although these methods might be effective to represent the dynamic model of the gas sensor, only the slow dynamics were focused on in the literature.[105,106] It is interesting if faster dynamics around a second is studied.

3.4. Frequency Analysis

Frequency analysis is useful when we try to extract information from the transient response as much as possible. Amrani et al. reported that the frequency characteristic of dissipation factor of a conducting polymer gas sensor had the information of gas discrimination.[108] The vapor in the headspace above the liquid was flowed to the sensor cell, and the dissipation factor was measured using an impedance analyzer. The measurement data of the acetone−methanol binary mixture is shown in Figure 40. It was found that the spectrum changed according to the composition. They said that the spectrum information was useful for the quantification of the multiple components even if only a single sensor was used.

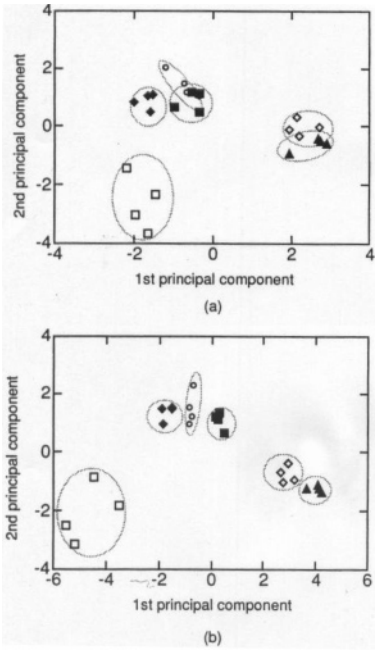

Figure 38. PCA diagram of (a) only normalized saturation-mass vector and (b) normalized saturation-mass vector and time-constant vector. Gases are acetone (○), 2-butanone (■), methanol (□), ethanol (◆), benzene (◇), and toluene (▲). Concentration of each sample ranges from 30 to 3000 ppm. Reprinted with permission from ref 102. Copyright 1993 IEE of Japan.

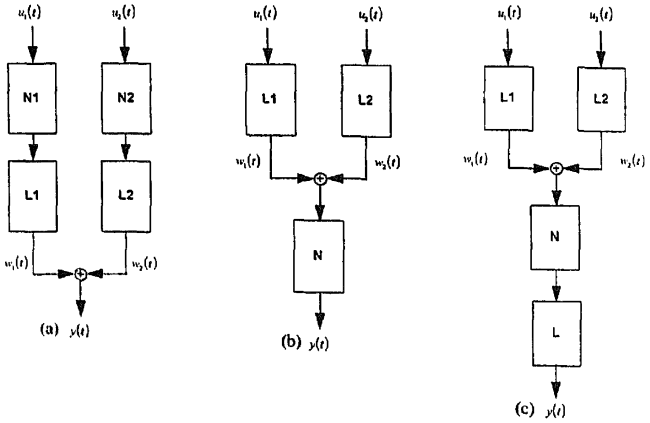

Figure 39. Several possible block-structured models of a sensor response to binary gas mixture. Reprinted with permission from ref 105. Copyright 1996 Elsevier Science.

The multiexponential models such as Gardner transform, METS (multiexponential transient spectroscopy), Pade−Laplace, and Pade-Z were applied to the analysis of conducting polymer gas sensor responses. It was reported that Pade−Laplace and Pade-Z models had better resolution capabilities than the other two methods.[109]

Fourier analysis and wavelet transform were often used to analyze the signals of the temperature-modulated gas sensors including the normal semiconductor gas sensors and microhotplate sensors.[110−112] Spectrum analysis is effective to extract the feature of the waveform. However, most of

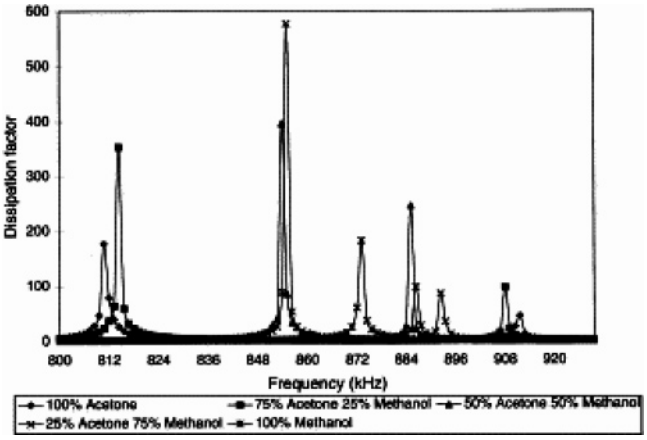

Figure 40. Frequency characteristic of dissipation factor of conducting polymer gas sensor. Reprinted with permission from ref 108. Copyright 1998 Elsevier Science.

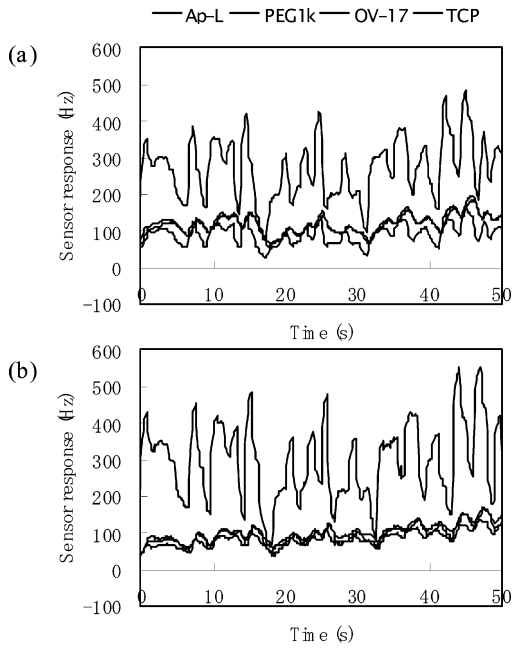

Figure 41. Sensor responses to odors in dynamically changing concentrations (a) apple and (b) Muscat flavors. Reprinted with permission from ref 113. Copyright 2007 Elsevier Science.

those methods have been used to analyze the vapor with the fixed concentration profile such as the step change.

Spectrum analysis technique can be used to enhance the robustness against the dynamic plume behavior.[113] The irregular change of the gas concentration occurred at the plume, whereas the concentration is stable in the closed system. The irregular changes of the gas concentrations of apple and Muscat flavors are shown in parts a and b of Figure 41. PCA diagram (not shown here) reveals that there was no separation between apple and Muscat flavors when only the magnitudes of the sensor responses were used in the open field with the plume. Although the time constant of apple flavor is different from the Muscat one, it is impossible to extract the time constant under the irregular change of the concentration in the time domain.

Thus, the Fourier analysis method was applied. Since the concentration changes irregularly and rapidly, the spectrum of the gas concentration approaches white noise. In this situation, a gas sensor works as a LPF (low-pass filter). Thus,

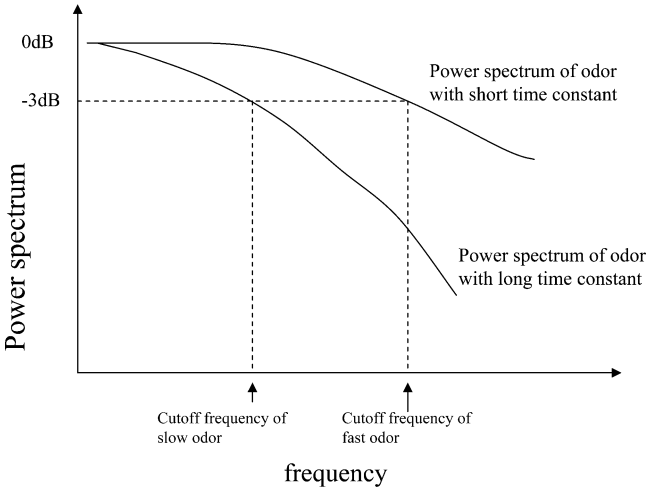

Figure 42. Concept of robustness enhancement against plume behavior using short-time Fourier transform.

the time constant in the time domain corresponds to the cutoff frequency in the frequency domain. This concept is illustrated in Figure 42. When the time constant is different, a different cutoff frequency is obtained, even under the irregular and rapid change of the gas concentration. Good pattern separation is obtained if the appropriate frequency component is selected.

Moreover, the real-time odor classification is required in the actual situation. Since many sampling points are typically required for the spectrum analysis, it takes much time to collect the data. The short-time Fourier transform (STFT) is the pseudo-real-time technique where the data in the moving window are used for the analysis. The spectrum $S(m,\omega)$ at time m in the discrete form is

$$S(m,\omega) = \sum_{n=-\infty}^{\infty} s[n]w[n-m]\, e^{-j\omega n} \qquad (26)$$

where $w[n]$ is the window function and n and m are integers. $s[n]$ is the sensor response signal in the time domain. One of the window functions is Hann Window, expressed as

$$w(n) = 0.5\left(1 - \cos\left(\frac{2\pi n}{N-1}\right)\right), \quad 0 \le n \le N-1 \qquad (27)$$

where N is the window width in the discrete form.

Several frequency components were used as elements of a vector for training and estimation. However, the discrimination became unstable when too many frequency components were used. Thus, the window width in ref 113 was just 4 s including 32 measurement points. The window moves every $^1/_8$ s. Furthermore, the variable selection based upon the discrimination analysis with Wilks' lambda[114,115] was performed to find the optimal frequency components. Only 2 variables among 64 were selected (4 sensors $\times$ 32 points/2). This result is shown in Figure 43. There is no information loss in this diagram because the data is two-dimensional after the variable selection. It is clear that the pattern separation is considerably improved when the STFT approach is adopted. Then, LVQ (learning vector quantization) was used to classify the samples.[116] The reference vectors of LVQ almost reflected on the data distribution after training, as is shown in Figure 43. As a result, >90% of the recognition probability was achieved after the improvement.

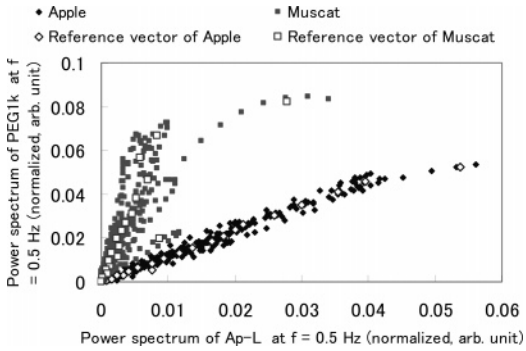

Figure 43. Pattern vectors obtained using STFT followed by variable selection and reference vector of LVQ after training. Sensing films are Ap-L (Apiezon L) and PEG (polyethylene glycol) 1000. Reprinted with permission from ref 113. Copyright 2007 Elsevier Science.

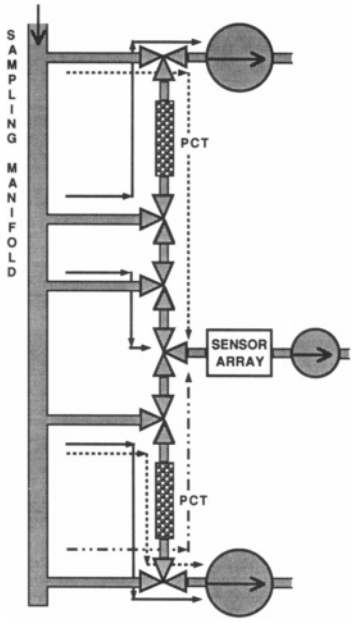

Figure 44. Schematic diagram of the sampling system with dual preconcentrator tubes, where PCT indicates preconcentrator tubes and the circles indicate the pump. Reprinted with permission from ref 117. Copyright 1993 American Chemical Society.

3.5. Temporal Data for Preconcentrator

In this section, the temporal information includes that of the sample discrimination, whereas the sensor dynamics has been described in the earlier subsection. Here, a preconcentrator with variable temperature is used.

The preconcentrator is typically used to enhance the sensor sensitivity.[117−120] Grate et al. proposed the system of a SAW sensor array combined with a preconcentrator. The dual preconcentrator tube system is shown in Figure 44. The upper PCT (preconcentrator tube) was operated on a 2 min cycle, while the lower one was operated on a 14 min cycle. The vapor collection during the 14 min cycle enabled more sensitive detection, whereas a longer response time was required. Sample airflow directions are indicated by the arrows, where the solid line indicates direct sampling, the dashed line indicates delivery of the preconcentrated sample from the upper PCT to the sensor array, and the dashed−dotted line shows delivery of preconcentrated sample from the lower PCT. The preconcentrator tube consisted of a $^1/_4$ in. o.d. by $^1/_8$ in. i.d. glass tube packed with 40−60 mesh Tenax GC over approximately a $^1/_4$ in. length of the tube.

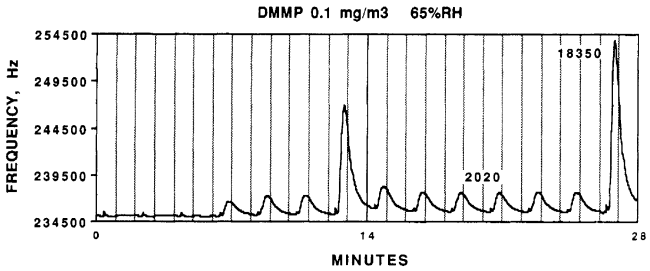

Figure 45. Response of SAW gas sensor (FPOL) to DMMP. The response is followed through two complete 14 min sampling periods. The numbers of 2 020 and 18 350 indicates the peak heights in Hz of 2 min and 14 min PCT mode responses. Reprinted with permission from ref 117. Copyright 1993 American Chemical Society.

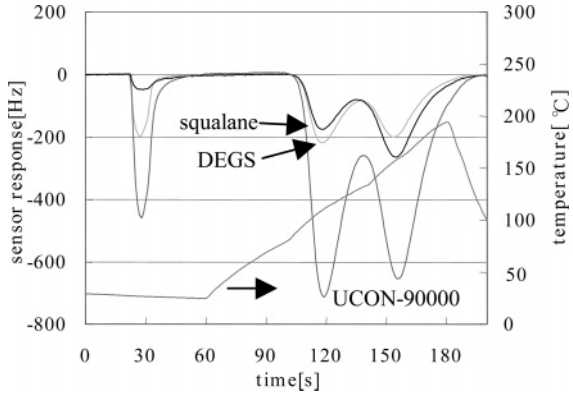

Figure 46. Sensor responses to binary mixture (butyl acetate and hexyl acetate) under gradual increase in temperature of preconcentrator. Reprinted with permission from ref 122. Copyright 2000 Elsevier Science.

The coil of nichrome wire wrapped around the glass tube provided the heat for thermal desorption. Figure 45 shows the sensor response to DMMP (dimethyl methylphosphonate) when both 2 min and 14 min cycles were adopted. It was found that the sensor response became larger as the vapor collection time increased.

It was also found that the gradual increase in the temperature of the preconcentrator enables the higher-order sensing,[121] including both distinguishable waveform and sensor-array output patterns, although the heat pulses with various temperatures were previously applied to the preconcentrator.[122]

One of the examples is shown in Figure 46.[123] The three QCM gas sensors coated with DEGS (diethylene glycol succinate), squalane, and UCON90000 were used together with the adsorbent Tenax-TA. The sample was the binary mixture of hexyl acetate and butyl acetate. The first peak around 30 s should be ignored since the sensor responded to the vapor not accumulated at the preconcentrator. The ramp of the temperature from room temperature to 200 °C started at 60 s and stopped at 180 s. The peak occurred at the desorption temperature of the corresponding compound. It was found that two peaks corresponding to butyl acetate and hexyl acetate were observed. This separation provides the enriched information for the pattern recognition.

Figure 47 shows the grayscale images of six sensor responses to apple flavors with various recipes. The waveforms of six sensors for 60 s are shown in the figure. The white portion means a large sensor response, whereas the black portion has no sensor response. The apple flavor was composed of four components: trans-2-hexenyl acetate

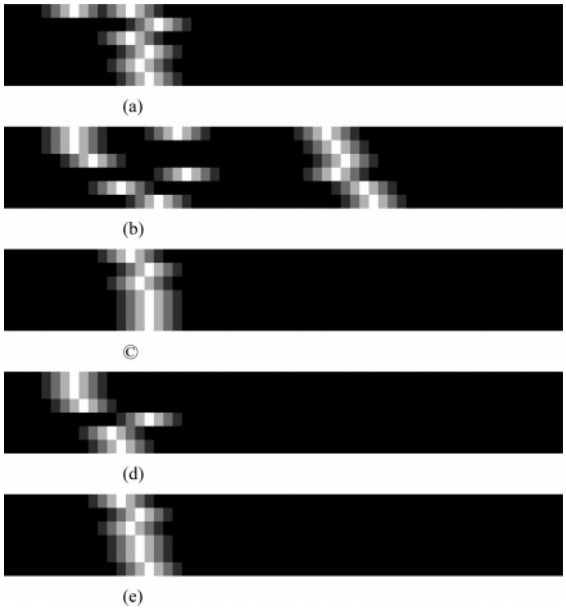

Figure 47. Image of six sensor responses to apple flavors with various recipes: (a) image of typical one, (b) image of enhanced green note, (c) image of enhanced smell of grass, (d) image of enhanced sour sweet, and (e) image of enhanced fruity note. Reprinted with permission from ref 123. Copyright 2005 IEEE.

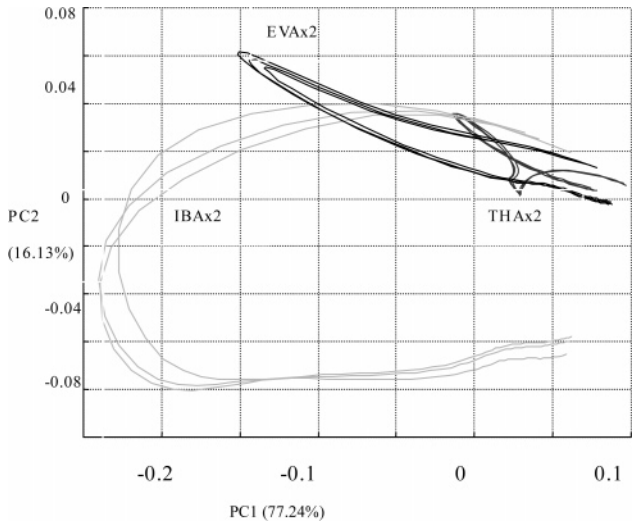

Figure 48. Loci of sensor responses to apple flavors with various recipes on PC1−PC2 plane obtained using PCA. Reprinted with permission from ref 123. Copyright 2005 IEEE.

(THA, softly green note), trans-2-hexenal (THL, smell of grass), isobutyric acid (IBA, sour sweet), and ethyl valerate (EVA, fruity note). In parts b−e of Figure 47, the enhanced note indicates that the portion of the corresponding compound in the mixture was twice increased. It was found that those samples with different recipes were easily discriminated using those images.

Moreover, the time courses of the sensor responses (six-dimensional data for 60 s) of three samples are projected onto the space obtained from the PCA, as is shown in Figure 48. THA × 2, IBA × 2, and EVA × 2 indicates enhanced green note, enhanced sour sweet note, and enhanced fruity note, respectively. Every sample was measured three times. Since the loci of the six different sensors have different features, those might be identified using a character-recognition technique.

The preconcentrator with variable temperature of the gradual ramp is effective to obtain rich information of the sample. The second-order data obtained from the preconcentrator with variable temperature in combination with the sensor array can be regarded as images. Each image of apple flavor with different composition was clearly distinguishable using the preconcentrator with variable temperature.

4. Sensing in Both Spatial and Time Domains

In this section, we review sensor array systems that involve sensing in both spatial and time domains. As shown in section 3, there are a variety of works devoted to the analysis of chemical sensor data in time domain, since such analysis is helpful in almost all applications of chemical sensors. In any systems equipped with chemical sensors, we have to deal with transient responses even if the intention is just to wait for the sensor signals to reach their steady states. On the other hand, spatially distributed sensor arrays were developed to measure spatial distributions of chemical substances, as described in section 2. However, only a limited number of works were so far addressed to combining the sensing and signal processing both in spatial and time domains. This is partly because working in a single domain is already complicated enough. For sensing in either domain, there is no established method that you can always rely on, and therefore, there are a lot of things to be done. Nonetheless, sensing in both spatial and time domains is extremely beneficial in some applications and provides information that cannot be obtained by sensing in a single domain.

4.1. Observing Change in Spatial Chemical Distribution with Time

The most straightforward examples in which both spatial and temporal features of chemical sensor signals are dealt with are the gas sensor arrays for measuring the spatial distribution of a chemical substance. How a chemical substance spreads in the given environment can be analyzed by observing the change in the measured spatial concentration distribution over time. When Yamasaki and Hiranaka reported their gas sensor array system, the demonstrations on measuring the growth of ethanol and ethyl ether gas clouds were presented in their paper.[8,9] A sequence of gas distribution maps was obtained by measuring the gas sensor responses at 1 s interval. Although this would be the best way to measure the entire gas distribution in a given environment, the number of sensors required is the problem if a large area is to be covered with high spatial resolution. The problem will be alleviated if the sensor data can be collected through a wireless network. The sensor network technology is reviewed in another paper in this special issue.[124]

The olfactory video camera was developed in a complementary approach. A highly packed small sensor array was fabricated to measure the gas flow over the sensor array, as shown in section 2.3.2. The direction of the gas flow was estimated by comparing the successive snapshots of the gas concentration distribution. The position of the gas source was localized by reversely tracking the observed gas flow. To make this approach work, care should be taken about the temporal resolution. The response and recovery times of the gas sensors must be short enough to observe clouds of gas passing over the small sensor array. Otherwise, all sensors respond and recover at the same time. The maximum

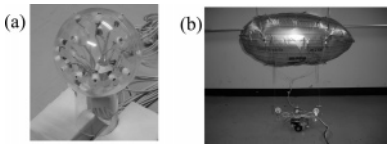

Figure 49. (a) Spherical gas sensor array for the measurement of three-dimensional gas flow. Twenty-one gas sensors are placed on a plastic sphere of 17 cm in diameter. (b) Tethered blimp robot. The direction of the gas source is estimated from the responses of 10 gas sensors attached on the 90 cm long balloon. A wheeled tractor robot changes the elevation and the position of the balloon so that it gradually approaches the source location.

measurable speed is higher for a larger sensor array since the difference in time for a gas cloud to reach the upstream and downstream edges of the sensor array becomes larger. However, introduction of a large sensor array in an environment alters the local airflow field around the sensor array.

Another problem of the packed gas sensor array is that it can measure the gas flow only when the array is placed along the flow direction. When the flow comes down vertically against the horizontally placed sensor array, for example, a complicated turbulent flow field is created around the sensor array. The sensors no longer respond in an ordered way to the gas clouds. A spherical gas sensor array shown in Figure 49a was fabricated to overcome this problem.[125] The spherical shape was chosen because of the symmetry in every direction. As an extension of the same technique, a blimp robot having a spheroidal sensor array was later developed (Figure 49b).[126] For those sensor arrays, however, a limited number of sensors were placed rather sparsely because of the difficulty in fabricating a large sensor array using the commercially available gas sensors. The gas flow cannot be measured when gas clouds flowing along the surface of the sensor array are smaller than the spacing between the gas sensors. When the microsensor technology advances to a point where fabrication of a dense array of fast gas sensors is enabled, the spherical sensor array will become a useful tool for locating gas sources by tracking gas plumes three-dimensionally.

Spatially distributed chemical sensor arrays can be used for applications other than localizing chemical sources. Sawada et al. proposed to use gas sensor units distributed in a house to monitor the activity of a resident.[127] Each sensor unit consisted of four different semiconductor gas sensors. The purpose of the monitoring system is to dispatch a medical team to the house when something happens to the resident. If an elderly person living alone in a house becomes seriously sick, he/she may not be able to ask for help by him/herself when the symptom has manifested. Various gaseous chemical components are generated in our daily activities, e.g., cooking, and in our metabolism. No activity in the gas sensor signal means that there is no activity of the resident. Another interesting application of gas sensor arrays is to place a sensor array in a plastic model of a canine nasal cavity.[30] The interiors of vertebrate nasal cavities, in which the olfactory receptor cells are distributed, generally have complicated structures. As the inhaled air goes thorough the cavity, gaseous components are separated since the cavity acts in a similar way to a gas chromatography column. Moreover, the complicated flow paths in the nasal cavity cause uneven distribution of odorants to the olfactory receptor cells. Odor molecules with different sizes and diffusion rates are delivered differently to the receptor cells at different locations. Stitzel et al. fabricated a nasal cavity model in which the complicated structure of a canine nasal cavity was precisely replicated based on the geometric data obtained using computed tomography scans of a real nasal cavity. Five fiber-optic vapor sensors were placed in the double-sized model. Although the same types of sensors were used, the time courses of the sensor responses were different when an odor pulse was supplied to the nasal cavity model. A unique spatial and temporal response pattern was obtained for a specific odorant, even though a single sensor type was used. The odor-discrimination capability of electronic noses can be, therefore, improved by placing sensors in the nasal cavity.

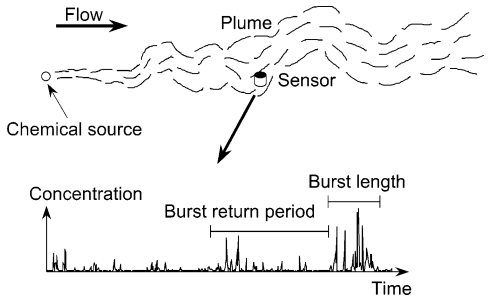

Figure 50. Intermittent and spiky signal from a stationary chemical sensor placed in a plume. Burst length is defined as the time between the leading and trailing edges of a burst of concentration spikes. Burst return period is defined as the time between the leading edges of two successive bursts. Peaks much higher than the mean concentration are often observed even at far downstream locations because of the sporadic and spiky nature of the chemical signal.

4.2. Correlating Signal Features in Time Domain with Spatial Locations

The sensor arrays presented in the previous section were designed to measure the spatial features of the chemical signals and to observe their temporal change. There are works that pursue the opposite approach, i.e., to measure the temporal features of the chemical signal and correlate them to the spatial locations with respect to the chemical sources.[128−133] A chemical plume has a patchy structure since eddies contained in the turbulent flow stretch and twist the streaks of the chemical substance.[134] A series of patches traveling over a stationary chemical sensor is represented as a spiky fluctuating signal in the time domain (Figure 50). The fine structure of the plume is the result of diffusion and turbulent mixing acted on the patches of a chemical substance released from the source. Temporal fluctuations of the signal thus convey some information about how the patches have been transported from their source to the location of the sensor. If such information can be decoded from the sensor signal, it can be exploited to estimate the location of the chemical source from a remote place. Although there is no clear evidence, there is a possibility that animals are using the information encoded in the fluctuating signals when they are in pursuit of smells.

The signal fluctuation contains a wide range of frequency components. One of the distinct characteristics of turbulent flow is that it contains a number of eddies of a variety of lengths scales.[134] The size of the largest eddies is determined by the geometrical dimension of the flow, which can reach hundreds of meters for large-scale plumes in the fields. The kinematic energy of such large eddies is cascaded to successively smaller eddies to the point at which the eddies get so small that they are damped by the viscosity. The size

of the smallest eddies is, thus, represented by the Kolmogorov length scale, η,

$$\eta \approx (\nu^3/\epsilon)^{1/4}$$

where ν is the kinematic viscosity of the fluid and ϵ is the rate of energy dissipation per unit mass. The Kolmogorov length scale is typically ~1 cm for the atmosphere[128] and was 0.7 mm[134] for the open-channel water flow with the depth of 20 cm and the mean velocity of 5 cm/s. Eddies larger than the plume width make the plume meander. On the other hand, eddies smaller than the plume width stir the edges of the plume with surrounding clean fluid medium and, thus, contribute to form the fine internal structure of the plume. Those structural features are observed as signal fluctuations with long and short periods, respectively. Therefore, in order to fully investigate the structure of the plume, a long record of chemical concentration needs to be measured at a high sampling rate. The time scale of the lowest-frequency component is typically several minutes for most of the flow regimes of interest. The time scale for the highest-frequency component can be estimated by calculating the time for an eddy with the size of the Kolmogorov length scale to pass over the sensor. Typical values are 1 ms for the atmosphere[128] and 0.1 s for the water flow mentioned above.[134] The discussion on the length and time scales so far was made solely on the velocity field. In reality, however, the concentration in a single eddy is not homogeneous. The Batchelor scale, L_B, represents the length scale of the smallest concentration patch[134] and is defined as

$$L_B \approx (\nu D^2/\epsilon)^{1/4}$$

where D is the molecular diffusion coefficient. The structure of the concentration distribution smaller than the Batchelor scale is immediately faded out by molecular diffusion. The Batchelor length scale is generally much smaller than the corresponding Kolmogorov scale since the molecular diffusion is a slow process. For the above-mentioned open-channel water flow, the Batchelor scale was only 0.02 mm.[134]

The currently available chemical sensors are not fast enough to resolve the fine-scale structure of chemical plumes. Therefore, for analyzing the plume structure, passive tracers that can be easily detected with high-speed sensors were used instead of real chemical substances. The basic nature of turbulent plumes is the same in airflow and in water flow. A laser-induced fluorescent technique was often used to observe the underwater chemical plumes.[130−132] In this technique, an aqueous solution of a fluorescent dye is released in the flow as a tracer, and the laser light sheet is shed to illuminate a cross section of the plume. The density of the dye solution is adjusted to be equal to the background water by adding the appropriate amount of another inert and lighter chemical substance like ethanol. Two-dimensional concentration distribution can be measured by recording the image of the induced florescent light, since its intensity is proportional to the local concentration of the dye. In some works, dopamine was used in conjunction with a high-speed electrochemical sensor, although this is a technique for point measurement.[129] The optical visualization technique described in section 2 has been applied so far to the measurement of aerial plumes up to 30 frames/s, although the Kolmogorov time scale of typical aerial plumes is ~1 ms. Extremely strong illumination is required for video recording with higher speed. Moreover, particles that are large enough to create bright images are no longer passive because of the significant mismatch of the density between the air and the tracer particles. Therefore, ionized air was used as a tracer for high-speed quantitative measurement.[128] Although the time resolution in the order of 1 ms can be achieved using this techniques, it provides the time record of chemical concentration only at a single point. The data on chemical distribution is not available. A high-speed photoionization detector was also used for measuring aerial plumes.[133]

Since a turbulent plume has a patchy filamentous structure, bursts of concentration spikes are observed when a stationary sensor is placed in the plume (Figure 50). Also, the plume meanders as a whole. Therefore, a single burst starts when the plume comes to the location of the sensor. The burst stops when the plume moves away from the sensor. The result is a series of bursts with periods of no signal between the bursts. Research efforts were made to investigate which features of the fluctuating signals can be used to track chemical plume as animals do. The gradient of instantaneous concentration is chaotic since the plume has a patchy structure. The gradient of time-averaged concentration can be used to track the plume. However, the problem is that the gradient is small, especially in the direction parallel to the flow. Moreover, it takes at least several minutes for the mean of the measured instantaneous concentration to converge to a statistically sound value. Other features of the time-series chemical signals investigated in the literature include burst length,[128,133] burst return period,[128,133] signal intermittency,[128,130,133] peak-to-mean ratio,[128,133] and rising slope of the concentration spikes.[129,133] However, what features animals use for plume tracking and what feature is the most reliable one for human or robotic searchers are still open questions. How the values of these features change with the sensor location depends not only on the flow characteristics, e.g., the turbulent intensity, but also on various parameters of the experimental setup, e.g., the size of the chemical source and the detection limit of the sensors. Therefore, contradicting results were often reported for different experimental setups.

The general conclusions are as follows, although it is difficult to summarize the work done so far for the above-mentioned reason. As a chemical plume extends downstream from the source location, the width of the plume itself and that of the plume meandering both increase. This results in the increase in burst length and burst return period at locations farther away from the source, although the increase is not always significant.[128] If a pair of sensors is placed across the flow direction, cross-correlation of the signals from the two sensors increases with the distance from the source because of the expansion of the plume width.[132] If a chemical substance is continuously released from the source, the signal is also continuous when the sensor is close to the source. As the plume becomes patchy and meandering as it travels, the signals at far locations generally become more intermittent.[133] However, as the patches of a plume are carried by the flow, their edges are mixed with the surrounding fluid medium by the small eddies contained in the turbulent flow. Molecular diffusion also makes those patches grow. These effects make the signal less intermittent. Therefore, in some case, the signal intermittency decreases with the distance from the source.[133]

The response time of the chemoreceptors of the animals is in the order of 0.1 s and is not sufficient to fully resolve the fine structure of chemical plumes.[129,133] However, there

is a possibility that the response characteristics of the chemoreceptors are serving as temporal filters to enhance the reception of specific features of the signals.[129] For example, the chemoreceptors show adaptation to sustained stimuli and respond more significantly to changing stimuli. Even if the mean concentration stays the same, the chemoreceptors respond in different ways to chemical stimuli with different intermittencies or different rising slopes of the peaks.

4.3. Frequency Analysis of the Chemical Signals in Plumes

As described in the previous section, streaks of a chemical substance released from the source are stretched and twisted by the eddies contained in the turbulent flow as the chemical streaks are carried downstream. The fine structure of the plume is thus created, and the fluctuating signal is obtained from a stationary chemical sensor. There is a possibility that the fluctuating signal contains some information about how the streaks are transported from the source to the location of the sensor. If the flow at some point between the chemical source and the sensor has distinctive characteristics, a particular structure is formed in the plume. The time course of the sensor signal then comes to have a corresponding signature. Detection of such a signature will be quite useful in the search for chemical sources. By analyzing the sensor signal, we might be able to tell on which route the chemical substance was transported.

One of the signatures that might be found in the plumes is periodic modulation of the chemical concentration. When a blunt object like a cylinder is immersed in a flow, it is known to periodically generate vortices with alternate rotation in its wake. The vortices are shed into the flow and form two staggered rows known as a Kármán vortex street.[135] In the case of a cylinder, the shedding frequency, f_s, is represented as

$$f_s = \frac{SU}{d} \tag{28}$$

where U is the flow velocity and d is the diameter of the cylinder. S is a nondimensional parameter called the Strouhal number, which is known to be constant (0.21) for a wide range of Reynolds numbers. When a chemical substance is released in the Kármán vortex street, an oscillatory plume is created. The introduction of the plume oscillation can be regarded as frequency modulation from the signal-processing perspective. A female moth releases a sexual pheromone, and a male moth tracks a plume of sexual pheromone to find a mate. When a female is perching on a branch of a tree, an oscillatory plume might be generated due to the Kármán vortex street in the wake of the branch or the trunk of the tree. A chemical plume released from a barrel may have a similar oscillating structure.

Mafra-Neto and Cardé investigated the difference in the moth's behavior in a continuous plume and in an oscillatory plume.[136] A 3 × 3 cm plastic deflector was placed 4 cm downstream from a pheromone-impregnated filter paper to generate an oscillatory plume. A continuous plume was generated in a similar way but without the plastic deflector. It was found that male moths, *Cadra cautella*, take straighter paths to the pheromone source in the oscillatory plume than in the continuous plume. In order to track a pheromone plume, a male moth surges in the upwind when in contact with a plume. When the contact is lost, the male starts zigzagging across the wind to find the lost plume. The results of the behavioral observation suggest that a fluctuating signal is required for sustaining the upwind progress toward the source. It should be noted that there is no direct evidence showing that moths detect the periodicity of the chemical signal. There is a possibility that the behavioral change was evoked in response to other properties of the chemical signal, e.g., the intermittency, since such properties also changed when the oscillation was introduced.

Justus et al. generated a similar oscillating plume by placing a circular disk immediately downstream from the source location.[133] A 3 m long and 1 m wide wind tunnel was prepared, and the wind speed was set to 50 cm/s. In their wind-tunnel setup, 1000 ppm of propene was released from the tip of a pipet, and a disk of 3.5 cm in diameter was placed perpendicular to the flow at 2.5 cm downstream from the pipet. The concentration of the tracer was recorded at various locations in the wind tunnel using a fast-response miniature photoionization detector with a sampling rate of 330 Hz. The frequency analysis was performed on the signals recorded in the oscillatory and continuous plumes. The power spectral density plot showed that the chemical signals in both plumes have a widely distributed spectrum due to the variety in sizes of the eddies contained in the turbulent flow. However, noticeable peaks were found in the power spectral density plot of the signal recorded immediately downstream (100 mm) from the source of the oscillatory plume. The frequencies of the peaks match the rate of the Kármán vortex generation. Those frequency components decayed rapidly over the distance. At 400 mm from the source, the peaks were almost buried in the background spectrum.

Kikas and co-workers proposed the use of an array of chemical sensors to detect frequency modulation introduced into chemical signals.[137−139] Signal fluctuation caused by the background turbulence contains a wide range of frequency components. The idea was to use correlation analysis to detect the small additional frequency component induced by the Kármán vortex street. When an array of sensors is placed in the frequency-modulated plume, the fluctuations of the sensor signals caused by the modulation should be correlated with each other. On the other hand, the fluctuations caused by small eddies in the background turbulent flow are uncorrelated. To find a correlated frequency component, the coherence spectrum[140] was calculated as

$$\gamma_{AB}(f) = \frac{|P_{AB}(f)|^2}{P_A(f)P_B(f)}$$

where $\gamma_{AB}(f)$ denotes the coherence between the signals from sensor A and B at frequency f. $P_A(f)$ and $P_B(f)$ represent the power spectral densities of the signals from sensor A and B, respectively. $P_{AB}(f)$ is the cross-power spectral density between the two signals. Coherence is an equivalent of a correlation coefficient in frequency domain. For a completely correlated signal, coherence has a value of 1. For a completely noncorrelated signals, the coherence becomes zero.

The idea was first tested using a benchtop apparatus called the "virtual plume", which is the combination of a simplified model of chemical transport in flow and real chemical sensors.[137−139] A chemical marker was released into water flow as a series of concentration pulses and was delivered to the electrochemical amperometric sensors through tubes

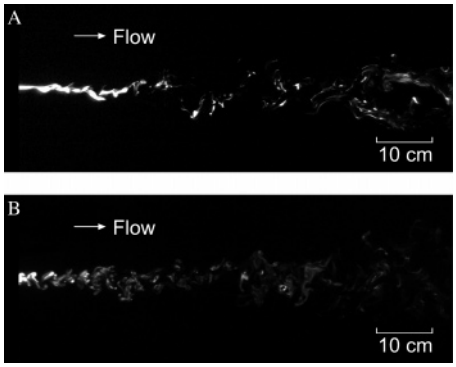

Figure 51. Grayscale calibrated instantaneous images of (a) unmodulated plume and (b) modulated plume. The size of the original images before cropping was 1018 × 1008 pixels for 1 m × 1 m field of view.

of different lengths. The sensors were shown to have sufficiently fast responses, and the 1 Hz pulsation could be detected in the coherence spectrum after the pulses were delivered through a 1 m long tube with a diameter of 0.5 mm. Later, the same coherence analysis was applied to the data of concentration fields measured in real chemical plumes using the laser-induced fluorescent technique. A small amount of fluorescent dye, Rhodamine 6G, was released in a water flow established in a 1.07 m wide, 24.4 m long tilting flume with rectangular cross section and smooth bed. The average velocity in the flume was 5.0 cm/s, and the flow depth was 20.0 cm. Sweeping an argon-ion laser beam in a plane parallel to the bed with a scanning mirror created the illumination sheet. The laser light caused the dye to fluoresce, and a digital CCD camera (8-bit grayscale, with 1018 vertical and 1008 horizontal pixels) captured the emitted light. The light intensity emitted by the dye is directly proportional to the dye concentration and laser intensity. However, the obtained raw images suffer from laser sheet nonuniformity, lens vignette, and pixel variability.[141] Therefore, an in situ calibration was performed to convert the raw images into quantitative data of concentration field. For the coherence analysis, 6000 images were captured with 10 frames/s. The field of view was 1 m × 1 m, and therefore, the spatial resolution was roughly 1 mm. The laser sheet was in the same horizontal plane as the plume source, 2.54 cm above the floor.

The frequency modulation was performed by placing a circular cylinder of 0.8 cm diameter at 2.54 cm downstream of the chemical source. Figure 51 shows the snapshots of unmodulated and modulated plumes. The periodic meanderings of the plume can be recognized for the modulated plume near the source. Figure 52a shows the power spectral density plot for the concentration on the centerline of the modulated plume at 5 cm downstream from the source. A small peak is recognized at 1.0 Hz, which roughly coincides with the frequency of the Kármán vortex generation. Figure 52b shows the coherence spectrum between the concentration on the centerline and at 1 cm to the side at 5 cm downstream from the source. Since the frequency modulation was generated by the organized lateral meanderings of the plume, it appears in the coherence spectrum as a correlated signal component at two laterally separated locations. The peak at the modulation frequency manifested itself clearly on the zero background. The peak decayed rapidly when the point of observation was moved downstream and disappeared at ~10 cm from the source. Therefore, when a dominant single

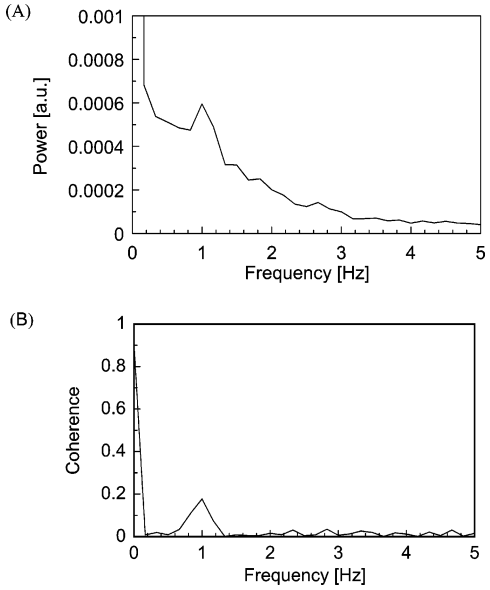

Figure 52. (a) Power spectral density of the time record of concentration at 5 cm downstream from the source in the modulated plume. (b) Coherence spectrum at the same location. The time record of concentration was taken from the same location as in (a) and the location 1 cm to the side.

peak is found in the coherence between sensors aligned across the flow, it means that the chemical source generating the Kármán vortex street is in close proximity. If the flow velocity is known, the size of the object can be calculated from the peak frequency. A robot with a visual sensor can start looking around for an object of that specific size. Although the frequency analysis provides us with useful information, its drawback is the need for long data to calculate accurate power spectra from random data. Moreover, most of the currently available chemical sensors are too slow to resolve the concentration fluctuations caused by the Kármán vortices. Development of more sophisticated signal-processing algorithms and high-speed chemical sensors is required to implement this technique in real applications.

5. Conclusion

In this paper, we described the aspect of chemical sensing in spatial and time domains and then reviewed the sensing related to both domains. Although sensing technology for chemical signals is not matured in comparison with that for physical signals, that technology is gradually proceeding.

In the study of spatial domain, the gas distribution can be measured using a homogeneous sensor array. Two types of sensor arrays, such as sparse and packed sensor arrays, are available. The sparse sensor array can show the global behavior of the plume, whereas the packed one reveals the local detailed behavior of the plume. The optical method is also useful to obtain the plume image. An attempt to make the plume generated in a virtual environment, where people perceive sensory stimuli even if they do not stay in the actual environment, is also introduced.

Next, a signal in time domain is described. Since the temporal information sometimes includes useful information for discriminating among the vapors, the technique to know the sensor dynamics such as time constant is studied. Frequency analysis is helpful when the useful information is hidden in the temporal data changing irregularly due to the turbulence.

Then, the sensing in both spatial and time domains is described. The straightforward method to understand the combination of both domains is to observe change in spatial distribution with time. Another approach is to see the correlation of signal features in time domain with several locations. The frequency analysis of the signals also provides us with useful information about an odor-source location.

It is an important task for us to fully understand the plume behavior in both spatial and time domains and to establish the measurement method of capturing its behavior. Moreover, a sensor dynamics model is required because a sensor response does not follow the speed of the plume change. A systematic approach including algorithms will become more important as well as the improvement of chemical-sensor capability itself. The current technology is not sufficient to find the toxic or explosive substance immediately. However, the appropriate combination of sensors with signal-processing techniques will make this a field in progress.

6. References

(1) Nakamoto, T.; Ishida, H.; Moriizumi, T. *Anal. Chem.* **1999**, *71* (15) 531A.
(2) Hinze, J. O.; *Turbulence*; McGraw-Hill: New York, 1975.
(3) Sutton, O. G. *Micrometeorology*; McGraw-Hill: New York, 1953.
(4) Pasquill, E.; Smith, F. B. *Atmospheric Diffusion*, 3rd ed.; Ellis Horwood: Chichester, U.K., 1983.
(5) Pal Arya, S. *Air Pollution Meteorology and Dispersion*; Oxford University Press: Oxford, U.K., 1999.
(6) Yamanaka, T.; Ishida, H.; Nakamoto, T.; Moriizumi, T. *Sens. Actuators, A* **1998**, *69*, 77.
(7) Tsujita, W.; Nakamoto, T.; Ishida, H.; Moriizumi, T. *Trans. IEICE Jpn.* **2002**, *J85-C*, 269.
(8) Hiranaka, Y.; Yamasaki, H. *IEE Jpn., Sensor Symp.* **1989**, 177.
(9) Yamasaki, H.; Hiranaka, Y. *Sens. Actuators, A* **1992**, *35*, 1.
(10) Ishida, H.; Suetsugu, K.; Nakamoto, T.; Moriizumi, T. *Sens. Actuators, A* **1994**, *45*, 153.
(11) Ishida, H.; Kagawa, Y.; Nakamoto, T.; Moriizumi, T. *Sens. Actuators, B* **1996**, *33*, 115.
(12) Ishida, H.; Kushida, N.; Yamanaka, T.; Nakamoto, T.; Moriizumi, T. *Trans. IEE Jpn.* **1999**, *119-E*, 194 (in Japanese).
(13) Ishida, H.; Yamanaka, T.; Kushida, N.; Nakamoto, T.; Moriizumi, T. *Sens. Actuators, B* **2000**, *65*, 14.
(14) Sharaf, M. A.; Illman D. L.; Kowalski, B. R. *Chemometrics* **1986**, 54.
(15) Sauerbrey, G. *Z. Phys.* **1959**, *155*, 289.
(16) King, W. H. *Anal. Chem.* **1964**, *36*, 1735.
(17) Hlavay, J.; Guilbault, G. G. *Anal. Chem.* **1977**, *49*, 1890.
(18) Kurosawa, S.; Kamo, N.; Matsui, D.; Kobatake, Y. *Anal. Chem.* **1990**, *62*, 353.
(19) Nakamoto, T.; Moriizumi, T. *Jpn. J. Appl. Phys.* **1990**, *29*, 963.
(20) Nakamoto, T.; Tokuhiro, T.; Ishida, H.; Moriizumi, T. *Tech. Dig. Transducers*'99 **1999**, 1878.
(21) Segawa, N.; Tokuhiro, T.; Nakamoto T.; Moriizumi, T. T. *IEE Jpn.* **2002**, *122-E*, 16 (in Japanese).
(22) Ishida, H.; Tokuhiro, T.; Nakamoto, T.; Moriizumi, T. *Sens. Actuators, B* **2002**, *83*, 256.
(23) Russell, R. A.; Thiel, D.; Deveza, R.; Mackay-Sim, A. *Proc. IEEE Int. Conf. Rob. Autom.* **1995**, 556.
(24) http://w-soramame.nies.go.jp.
(25) http://www.kankyo.metro.tokyo.jp.
(26) Maruo, Y. Y.; Ogawa, S.; Ichino, T.; Murao, N.; Uchiyama, M. *Atmos. Environ.* **2003**, *37*, 1065.
(27) Ohyama, T.; Maruo, Y. Y.; Tanaka, T.; Hayashi, T. *Sens. Actuators, B* **2000**, *64*, 142.
(28) Tsujita, W.; Yoshino, A.; Ishida, H.; Morrizumi, T. *Sens. Actuators, B* **2005**, *110*, 304.
(29) Settles, G. S. *J. Fluid Dyn.* **2005**, *127*, 189.
(30) Stitzel, S. E.; Stein, D. R.; Walt, D. R. *J. Am. Chem. Soc.* **2003**, *125*, 3684.
(31) Yokosawa, K.; Nakano, S.; Goto, Y.; Tsukada, K. *Proc. 22nd Sensor Symp., IEE Jpn.* **2005**, 435.
(32) Lundstrom, I.; Shivaraman, S.; Svensson, C.; Lindkvist, L. *Appl. Phys. Lett.* **1974**, *26*, 55.
(33) Bather, W. *Sens. Update* **1998**, *4*, 82.
(34) *Environmental Analysis Technology Handbook*, 5th ed.; GASTEC: Kanagawa, Japan, 2004.
(35) Tanaka, Y.; Yoshioka, M.; Nakamoto, T.; Moriizumi, T. *Trans. SM, IEE Jpn.* **2004**, *124*, 321 (in Japanese).
(36) Tanaka, Y.; Nakamoto, T.; Moriizumi, T. *Sens. Actuators, B* **2006**, *119*, 84.
(37) Ninh, H. P.; Tanaka, Y.; Nakamoto, T.; Hamada, K. *Sens. Actuators, B* **2007**, *125*, 138.
(38) Nakamoto, T.; Tanaka, Y.; Ninh, H. P. *Trans. IEE Jpn.* **2007**, *127*, 359.
(39) Yamanaka, T.; Matsumoto, R.; Nakamoto, T. *Sens. Actuators, B* **2002**, *87*, 457.
(40) Kulp, T. J.; Garvis, D.; Kennedy, R.; McRae, T. G. *Proc. SPIE* **1991**, *1479*, 352.
(41) Kulp, T. J.; Powers, P. E.; Kennedy, R. *Proc. SPIE* **1997**, *3061*, 269.
(42) Powers, P. E.; Kulp, T. J.; Kennedy, R. *Appl. Opt.* **2000**, *39*, 1440.
(43) Nagashima, T.; Yamashita, K.; Hatta, S.; Kajihara, R.; Hamakawa, Y.; Okuyama, M. *Tech. Dig. Sens. Symp., IEEJ* **2001**, 109.
(44) Ochiai, M.; Kuroki, M. Presented at Technical meeting on chemical sensor, IEE of Japan, 1998; Tokyo, CS-98-47.
(45) Yamada, T.; Yokoyama, S.; Tanikawa, T.; Hirota, K.; Hirose, M. *Proc. IEEE Virtual Reality* **2006**, 199.
(46) Nakamoto T.; Pham, H. D. M. *Proc. IEEE Virtual Reality* **2007**, 179.
(47) Gardner, J. W. *Sens. Actuators, B* **1990**, *1*, 166.
(48) Nakamoto, T.; Iguchi, A.; Moriizumi, T. *Sens. Actuators, B* **2000**, *71*, 155.
(49) Tobias, P.; Baranzahi, A.; Spetz, A. L.; Kordina, O.; Janzen, E.; Lundstrom, I. *IEEE Electron Device Lett.* **1997**, *18*, 287.
(50) Murlis, J.; Elkinton, J. S.; Carde, R. T. *Annu. Rev. Entomol.* **1992**, *37*, 505.
(51) Llobet, E., Pearce, T. C., Schiffman, S. S., Nagle, H. T., Gardner, J. W., Eds.; *Handbook of machine olfaction*; Wiley-VCH: New York, 2003; p 293.
(52) Hines, E. L.; Llobet, E.; Gardner, J. W. *IEE Proc. Circuits Devices Syst.* **1999**, 146 (*6*), 297.
(53) Tsujita, W.; Nakamoto, T.; Ishida, H.; Moriizumi, T. *Trans. IEICE* **2002**, *J85-C*, 269 (in Japanese).
(54) Rumelhart, D. E.; McClelland, J. L. *PDP Research Group Parallel Distributed Processing*; MIT Press: Cambridge, MA, 1986; Vol. 1, p. 318.
(55) Rumelhart, D. E.; Hinton, G. E.; Williams, R. J. *Nature* **1986**, *323*, 533.
(56) Duda, R. O.; Hart P. E.; Stork, D. G. *Pattern classification*; Wiley-Interscience: New York, 2001; p 287.
(57) Shumer, H. V.; Gardner, J. W. *Sens. Actuators, B* **1992**, *8*, 1.
(58) Weimar, U.; Schierbaum, K. D.; Goepel, W. *Sens. Actuators, B* **1990**, *1*, 93.
(59) Ionescu, R.; Llobet, E. *Sens. Actuators, B* **2002**, *81*, 289.
(60) Wilson, D. M.; Dunman, K.; Roppel, T.; Kalim, R. *Sens. Actuators, B* **2000**, *62*, 199.
(61) Afridi, M. Y.; Suehle, J. S.; Zaghloul, M. E.; Berning, D. W.; Hefner, A. R.; Cavicchi, R. E.; Semancik, S.; Montgomery, C. B.; Taylor, C. J. *IEEE Sens. J.* **2002**, *2*, 644.
(62) Arnold, C.; Harms, M.; Goschnick, J. *IEEE Sens. J.* **2002**, *2*, 179.
(63) Ema, K.; Yokoyama, M.; Nakamoto, T.; Moriizumi, T. *Sens. Actuators* **1989**, *13*, 476.
(64) Davide, F.; Natale, C. C.; D'Amico, A.; Hierlemann, A.; Mitrovics, J.; Schweizer, M.; Weimar, U.; Goepel, W.; Marco, S.; Pardo, A. *Sens. Actuators, B* **1995**, *26*−*27*, 275.
(65) Yano, K.; Yoshitake, H.; Bornscheuer, U. T.; Schmid, R. D.; Ikebukuro, K.; Yokoyama, K.; Matsuda, Y.; Karube, I. *Anal. Chim. Acta* **1997**, *340*, 41.
(66) Nakamura, M.; Sugimoto, I.; Kuwano, H.; Lemos, R. *Sens. Actuators, B* **1994**, *20*, 231.
(67) Carey, W. P.; Beebe, K. R.; Kowalski, B. R.; Illman, D. L.; Hirschfeld, T. *Anal. Chem.* **1986**, *58*, 149.
(68) Nakamoto, T.; Fukunishi, K.; Moriizumi, T. *Sens. Actuators* **1989**, *13*, 473.
(69) Nakamura, K.; Nakamoto, T.; Moriizumi, T. *Sens. Actuators, B* **1999**, *61*, 6.
(70) Nakamura, K.; Nakamoto, T.; Moriizumi, T. *Sens. Actuators, B* **2000**, *69*, 295.
(71) Nanto, H.; Subakino, S.; Habara, M.; Kondo, K.; Morita, T.; Douguchi, Y.; Nakazumi, H.; Waite, R. I. *Sens. Actuators, B* **1996**, *34*, 312.
(72) Muramatsu, H.; Tamiya, E.; Karube, I. *Anal. Chim. Acta* **1989**, *225*, 399.
(73) Ballantine, D. S.; Rose, S. L.; Grate, J. W.; Wohltjen, H. *Anal. Chem.* **1986**, *58*, 3058.
(74) Grate, J. W.; Wise, B. M.; Abraham, M. H. *Anal. Chem.* **1999**, *71*, 4544.
(75) Zellers, E. T.; Han, M. *Anal. Chem.* **1996**, *68*, 2409.
(76) Stahl, U.; Rapp, M.; Wessa, T. *Anal. Chim. Acta* **2001**, *450*, 27.

(77) Bender, F.; Barié, N.; Romoudis, G.; Voigt, A.; Rapp, M. *Sens. Actuators, B* **2003**, *93*, 135.
(78) Hagleltner, B.; Hierlemann, A.; Lange, D.; Kummer, A.; Baltes, H. *Nature* **2001**, *414*, 293.
(79) Battiston, F. M.; Ramseyer, J.-P.; Lang, H. P.; Baller, M. K.; Gerber, C. H; Gimzewski, J. K.; Meyer, E.; Güntherodt, H.-J. *Sens. Actuators, B* **2001**, *77*, 122.
(80) Cai, Q.; Park, J.; Heldsinger, D.; Hsieh, M.; Zellers, E. T. *Sens. Actuators, B* **2000**, *62*, 121.
(81) Hatfield, J. V.; Neaves, P.; Hicks, P. J.; Persaud, K.; Travers, P. *Sens. Actuators* **1994**, *18*−*19*, 221.
(82) Gardner, J. W.; Pearce, T. C.; Friel, S.; Bartlett, P. N.; Blair, N. *Sens. Actuators, B* **1994**, *18*−*19*, 240.
(83) Hassan, M. E.; Amrani, Dowdeswell, R. M.; Payne, P. A.; Persaud, K. C. *Sens. Actuators, B* **1997**, *44*, 512.
(84) Slater, J. M.; Paynter, J.; Watt, E. J. *Analyst* **1993**, *118*, 379.
(85) Doleman, A. J.; Lewis, N. S. *Sens. Actuators, B* **2001**, *72*, 41.
(86) Ryan, M. A.; Zhou, H.; Buehler, M. G.; Manatt, K. S.; Mowrey, V. S.; Jackson, S. P.; Kisor, A. K.; Shevade, A. V.; Homer, M. L. *IEEE Sens. J.* **2004**, *4*, 337.
(87) Hayes, A. T.; Martinoli, A.; Goodman, R. M. *IEEE Sens. J.* **2002**, *2*, 260.
(88) Sundgren, H.; Lundstrom, I.; Winquist, F.; Lukkari, I.; Carlsson, R.; Wold, S. *Sens. Actuators, B* **1990**, *2*, 115.
(89) Covington, J. A.; Gardner, J. W.; Briand, D.; de Rooij, N. F. *Sens. Actuators, B* **2001**, *77*, 155.
(90) Davide, F.; Andersson, M.; Holmberg, M.; Lundstrom, I. *IEEE Sens. J.* **2002**, *2*, 636.
(91) Pillonel, L.; Bosset, J. O.; Tabacchi, R. *Eur. Food Res. Technol.* **2000**, *214*, 160.
(92) Garrigues, S.; Talou, T.; Nesa, D.; Gaset, A. *Sens. Actuators, B* **2001**, *78*, 337.
(93) Morvan, M.; Talou, T.; Beziau, J.-F. *Sens. Actuators, B* **2003**, *95*, 212.
(94) Bindig, U.; Katzung, W.; Mauch, H.; Leonhardt, J.; Muller, G. *Tech. Dig. 9th Int. Symp. Olfaction Electronic Nose*; **2002**, 106.
(95) Staples, E. J. *Proc. IEEE Ultrason. Symp.* **1999**, 417.
(96) White, J.; Kauer, J. S.; Dickinson, T. A.; Walt, D. R. *Anal. Chem.* **1996**, *68*, 2191.
(97) Albert, K. J.; Walt, D. R. *Anal. Chem.* **2003**, *75*, 4161.
(98) Rakow, N. A.; Suslick, K. S. *Nature* **2000**, *406*, 710.
(99) Natale, C. D.; Salimbeni, D.; Paolesse, R.; Macagnano, A.; D'Amico, A. *Sens. Actuators, B* **2000**, *65*, 220.
(100) Stetter, J. R.; Jurs, P. C.; Rose, S. L. *Anal. Chem.* **1986**, *58*, 860.
(101) Nakamura, M.; Sugimoto I.; Kuwano, H. *IEEJ Chem. Sens. Meet.* **1997** *CS-97-37*, 21 (in Japanese).
(102) Nakamura, M.; Sugimoto, I.; Kuwano H.; Lemos, R. *Dig. Tech. Pap., Transducers'93* **1993**, 434.
(103) Nakamura, M.; Sugimoto, I.; Kuwano, H. *Dig. Tech. Pap. Transducers'95* **1995**, 795.
(104) Skogestad S.; Postlethwaite, I. *Multivariable Feedback Control*; Wiley: New York, 1996; p 1.
(105) Marco, S.; Pardo, A.; Davide, F. A. M.; Natale, C. D.; D'Amico, A. *Sens. Actuators, B* **1996**, *34*, 213.
(106) Davide, F. A. M.; Natale, C. D.; D'Amico, A.; Hierlmann, A.; Mitrovics, J.; Schweizer, M.; Weimar, U.; Goepel, W. *Sens. Actuators, B* **1995**, *24*−*25*, 830.
(107) Schweizer-Berberich, M.; Goeppert, J.; Hierleman, A.; Mitrovics, J.; Weimar, U.; Rosenstiel, W.; Gaepel, W. *Sens. Actuators, B* **1995**, *26*−*27*, 232.
(108) Amrani, M. E. H.; Dowdeswell, R. M.; Payne, P. A.; Persaud, K. C. *Sens. Actuators, B* **1997**, *44*, 512.
(109) Guitierrez-Osuna, R.; Troy, Nagle, H.; Schiffman, S. S. *Sens. Actuators, B* **1999**, *61*, 170.
(110) Nakata, S.; Okunishi, H.; Nakashima, Y. *Sens. Actuators, B* **2006**, *119*, 556.
(111) Ionescu, R.; Llobet, E. *Sens. Actuators, B* **2002**, *81*, 289.
(112) Vergara, A.; Llobet, E.; Brezmes, J. ; Ivanov, P.; Cané, C. ; Gràcia, I. ; Vilanova, X.; Correig, X. *Sens. Actuators, B* **2007**, *123*, 1002.
(113) Nimsuk, N.; Nakamoto, T. *Sens. Actuators, B* **2007**, *127*, 491.
(114) Dillon, W. R.; Goldstein, M. *Multivariate Analysis*; Wiley: New York, 1984; p 394.
(115) Nakamoto, T.; Sasaki, S.; Fukuda, A.; Moriizumi, T. *Sens. Mater.* **1992**, *4*, 111.
(116) Kohonen, T. *Self-organization and associative memory*; Springer-Verlag: New York, 1988; p 199.
(117) Grate, J. W.; Rose-Pehrsson, S. L.; Venezky, D. L.; Klusty, M.; Wohltjen, H. *Anal. Chem.* **1993**, *65*, 1868.
(118) Grooves, W. A.; Zellers, E. T.; Frye, G. C. *Anal. Chim. Acta* **1998**, *371*, 131.
(119) Kita, J.; Aoyama, Y.; Kinoshita, M.; Nakano, H.; Akamatsu, H. *Tech. Dig. IEEJ Sens. Symp.* **2000**, 301.
(120) Bender, F.; Barie, N.; Romoudis, G.; Voigt, A.; Rapp, M. *Sens. Actuators, B* **2003**, *93*, 135.
(121) Booksh, S.; Kowalski, B. R. *Anal. Chem.* **1994**, *66*, 782.
(122) Nakamoto, T.; Isaka, Y.; Ishige, T.; Moriizumi, T. *Sens. Actuators, B* **2000**, *69*, 58.
(123) Nakamoto, T.; Sukegawa, K.; Sumitomo, E. *IEEE Sens. J.* **2005**, *5*, 68.
(124) Diamond, D. *Chem. Rev.* **2008**, *80*.
(125) Ishida, H.; Tsuruno, M.; Yoshikawa, K.; Moriizumi, T. *Proc. 11th Int. Conf. Adv. Rob.* **2003**, 369.
(126) Ishida, H.; Zhu, M.; Johansson, K.; Moriizumi, T. *Conf. Proc., Int. Conf. Electr. Eng.* **2004**, *3*, 117.
(127) Sawada, A.; Oyabu, T.; Nanto, H. *Trans. IEE Jpn.* **2001**, *121-E*, 434.
(128) Murlis, J.; Elkinton, J. S.; Cardé, R. T. *Annu. Rev. Entomol.* **1992**, *37*, 505.
(129) Moore, P. A.; Atema, J. *Biol. Bull.* **1991**, *181*, 408.
(130) Liao, Q.; Cowen, E. A. *Environ. Fluid Mech.* **2002**, *2*, 9.
(131) Crimaldi, J. P.; Koehl, M. A. R.; Koseff, J. R. *Environ. Fluid Mech.* **2002**, *2*, 35.
(132) Weissburg, M. J.; Dusenbery, D. B.; Ishida, H.; Janata, J.; Keller, T.; Roberts, P. J. W.; Webster, D. R. *Environ. Fluid Mech.* **2002**, *2*, 65.
(133) Justus, K. A.; Murlis, J.; Jones, C.; Cardé, R. T. *Environ. Fluid Mech.* **2002**, *2*, 115.
(134) Roberts, P. J. W.; Webster, D. R. In *Environmental Fluid Mechanics: Theories and Application*; Shen, H. H., Cheng A. H.-D., Wang, K.-H., Teng, M. H., Liu, C. C. K., Eds.; ASCE Press: Reston, VA, 2002.
(135) White, F. M. *Viscous Fluid Flow*, 2nd ed.; McGraw-Hill: New York, 1991.
(136) Mafra-Neto, A.; Cardé, R. T. *Physiol. Entomol.* **1995**, *20*, 117.
(137) Kikas, T.; Ishida, H.; Webster, D. R.; Janata, J. *Anal. Chem.* **2001**, *73*, 3662.
(138) Kikas, T.; Janata, P.; Ishida, H. Janata, J. *Anal. Chem.* **2001**, *73*, 3669.
(139) Kikas, T.; Ishida, H.; Janata, J. *Anal. Chem.* **2002**, *74*, 3605.
(140) Kay, S. M. *Modern Spectral Estimation*; Prentice Hall: Upper Saddle River, NJ, 1988.
(141) Ferrier, A. J.; Funk, D. R.; Roberts, P. J. W. *Dyn. Atmos. Oceans* **1993**, *20*, 155.

CR068117E